Journal of Multifunctional Composites

journal homepage: http://jmc.destechpub.com

Hybrid Thin Film Lithium Ion-Graphite Composite Battery Laminates: An Experimental Quasi-static Characterization

FEDERICO GASCO* and PAOLO FERABOLI

Department of Aeronautics & Astronautics, University of Washington, Box 352400, Seattle, WA, 98195-2400, USA

KEYWORDS

Multifunctional structures
Energy harvesting
Energy storage
Smart structures

ABSTRACT

The concept of a multifunctional laminated composite airframe material for load bearing and electrical energy storage is proposed. The laminated structure is comprised of integrated solid state thin film lithium-ion batteries and carbon fiber/epoxy laminae. Mechanical and electromechanical tests were conducted in order to characterize the stress-strain field and determine the operational envelope of the hybrid laminate featuring the current thin film battery technology. The limits of applicability of classical analysis methods in mechanics of composite materials were assessed and several critical failure modes were determined to support the design of the next generation of airborne structural thin film batteries.

1. INTRODUCTION

The consolidation of batteries and airframe into a multifunctional structure can theoretically reduce the aircraft weight by exploiting the battery components as load bearing elements, by eliminating batteries supports and by enabling distributed power supply and storage, potentially reducing the amount of wiring. Currently sought-after for unmanned aerial vehicles (UAV), this design solution could lead to a significant improvement of the flight endurance of electrical propeller-driven aircraft [1,2]. To realize this vision, new constituents and a novel design of the composite material system have to be developed to enable simultaneous electrical energy storage and mechanical load bearing capabilities.

Research on lithium-polymer (Li-Po) batteries showed that elastic moduli and strengths of mechanically reinforced batteries as high as 1.02 GPa and 3.9 MPa respectively can be achieved, retaining a specific electrical energy of 160 Wh/kg [3,4]. These pioneering works proved the capability of the multifunctional airframe concept for a micro-UAV. However the lack of stiffness of the battery packaging [4], as well as the plasticized state of the relatively thick organic polymer electrolyte [5], compromises the mechanical properties of the current Li-Po technology. Furthermore today's available electrode materials, consisting of lithium intercalation compounds, are such that high specific energy and specific power, as well as good mechanical properties cannot be achieved [3,4,6,7]. In [6] a battery with an equivalent Young's modulus of 3.1 GPa was developed, whereas the specific energy dropped to 35 Wh/kg. The causes of the low electrochemical performance were the insufficient electrical capacity of the carbon nano-fiber reinforced lithium transition metal oxide cathode and the low ionic conductivity of the solid state polymer electrolyte. These multifunctional composites can lead to a system improvement for applications with either low mechanical or electrical demands. However, mechanical and electrical performances have to be simultaneously increased in order to fulfill the high specific modulus and strength, as well as the high specific electrical energy and power, required by a lightweight airborne application. The literature review gives evidence that improvements are needed not only in the multifunctional performance of the electrolyte and the electrodes, but also in the mechanical design of the composite structure.

Organic polymer electrolytes with engineered mechanical

*Corresponding author. Ph.: +1-206-979-6440. Fax: +1-206-543-0217;
Email: gasco@uw.edu

doi:10.12783/issn. 2168-4286/1.1/Gasco

properties have been studied for three decades as solid state electrolytes [5]. Their ionic conductivity is still inadequate to deliver the power density required by most conventional applications, explaining why they are exclusively employed in a gel state obtained by plasticizing them with the addition of liquid electrolytes, as confirmed by the most recent studies, like [8]. Notably in [9–11] the effects of constituents concentration and glass transition temperature, polymers chemistry and architecture on the electrolyte multifunctional properties were thoroughly investigated by synthesizing and analyzing a large variety of vinyl ester-based solid electrolytes and epoxy-based gel electrolytes. The study demonstrated and characterized the inverse correlation between ionic conductivity and elastic modulus, but it also showed a promising trend of increased multifunctional performance, with conductivities approaching the values required for thin film batteries.

Cathode materials are the limiting factor in today's battery systems in terms of specific capacity and specific power, due to their low rate of ionic diffusion and electronic conductivity. For this reason they typically have to be mixed with electrically conductive diluents [12,13]. Adding a large quantity of structural binder to the mixture, as needed to accomplish the load bearing function, causes the specific and volumetric electrochemical performances to drop even more. This is particularly undesirable for aeronautical applications.

The development of a structural anode seems to be a relatively easier task because available anode bulk materials have an intrinsically higher specific capacity than cathode materials. Above all are silicon and graphite, the latter being not only an intercalation material for lithium ions, but also an electrically conductive and structural material [7].

In order to meet the requirements for the next generation of airborne load bearing batteries, solid state thin film Li-ion batteries (TFB) with nanostructured electrodes were recently proposed [8,14–25], Figure 1. The thin film structure maximizes the specific contact surface between electrodes and electrolyte, thereby increasing the stored energy and power per unit mass by increasing the fraction of reactants and the rate of the electrochemical reaction respectively. In fact, downsizing the electrodes and electrolyte to a thin film dramatically reduces the path length for ionic and electronic transport, allowing to achieve the desired conductivity without utilizing diluents or micro-porous compounds [5,14].

Scalable manufacturing processes for nanostructured materials, such as electrospinning, chemical vapor deposition (CVD), atomic layer deposition (ALD) and others are suitable for TFB manufacturing. The future application of nano-scale technology to the electrode materials can potentially lead to several advantages. First, it enables further increase of TFB specific energy and power by decreasing the path length of Li-ion and electronic transportation, allowing full exploitation of the theoretical electrical capacity of the materials [14–18]. It can also implement energy storage and load bearing multifunctionality more efficiently than bulk materials, through engineered nanocomposites comprised of electrochemically active nanostructures bound by an electrically conductive reinforced composite. Lastly, nanostructured materials allow better accommodation of the cycling strain induced by the mechanical boundary conditions and by Li-ion insertion and removal. The latter is a known cause for low durability and capacity fading of electrode materials, in particular for silicon, which provides the highest capacity among the known anode materials [15,19–21]. However, nanostructured electrodes are not technology ready. Although several of such cathode materials were synthesized from lithium transition metal oxides, vanadium or manganese oxides and transition metal phosphates [14,17,18], as well as anode materials from silicon and graphite [8,15,16], none of them are commercially available. The reason is the complex synthesis, the low packing of particles and the occurrence of undesirable reactions with the electrolyte that undermines durability.

Finally, all the battery materials have to be solid state

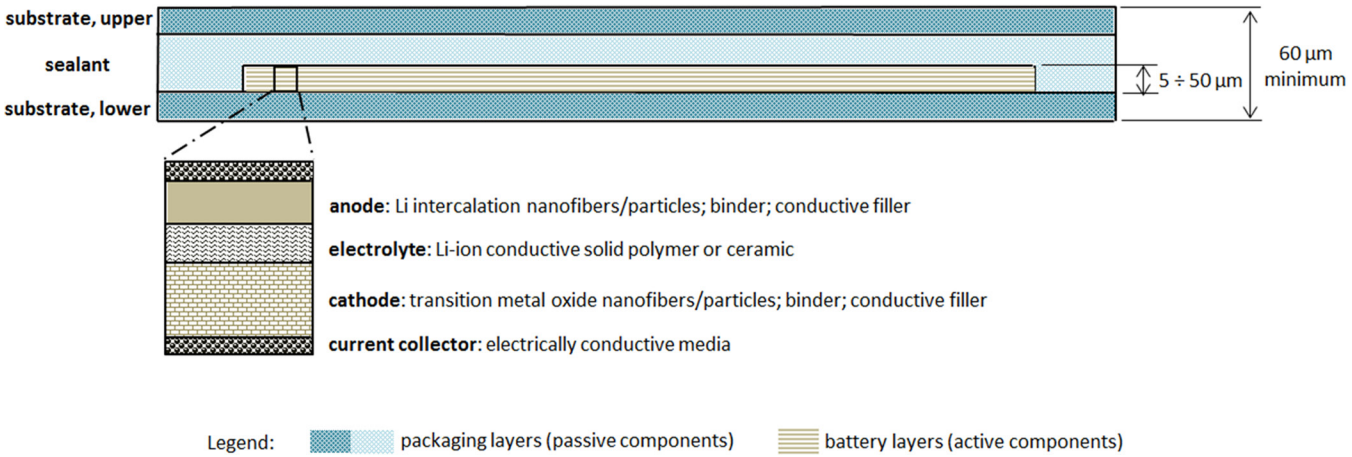

Figure 1. *Cross-sectional schematic of a next generation all-solid state thin film Li-ion battery (TFB). Typical thicknesses are indicated. Envisioned design is based on current research status on nanostructured electrode materials.*

to ensure three-dimensional continuity of the load path at any point within the structure, as the presence of discontinuities, such as porosity, voids or delaminations, is a major threat for the mechanical integrity of a composite laminate. Solid state batteries also ensure higher safety since they do not leak hazardous chemicals if a mechanical failure of the packaging occurs. In addition, the solid state electrolyte is also not combustible and does not suffer from thermal runaway, which can cause explosion of conventional lithium-ion prismatic batteries. Besides, a liquid electrolyte would not allow the manufacturing of a thin film cell because of its liquid surface tension and because of the need of a porous separator between the electrodes to avoid electrical shorting.

The low TFB thickness, typically less than 300 μm, facilitates the integration within thin sections and laminated composite structures, but it also implies that a significant weight fraction of the battery is constituted by the packaging layers. The simplest configuration of the battery packaging is comprised of three layers, Figure 1: a lower substrate provides mechanical support for the in-situ deposition process of the electrochemical cell components; a sealant layer ensures that the highly reactive and hygroscopic cell materials are sealed; an upper substrate provides an almost symmetric stacking sequence. Such a casing allows safe processing and lasting operation of the TFB outside of the deposition chamber, while providing in-plane strength and stiffness to the battery lamina.

The integration of TFBs and structural composite laminae, such as carbon fiber/epoxy (CFRP) plies, into a hybrid thin film lithium ion-graphite composite battery (TFB-CFRP) laminate poses manufacturing and design challenges. The compatibility of the commercial state-of-the-art TFB cell to the epoxy based composite curing pressures and temperatures was previously assessed by the authors. This electrochemical cell was comprised of a nanocrystalline lithium cobalt oxide ($LiCoO_2$) cathode, a ceramic LiPON ($Li_{2.9}PO_{3.3}N_{0.46}$) electrolyte and a metallic lithium (Li) anode, Figure 2 and Figure 3. The study, which is published separately, successfully determined the cure cycle and the TFB charge level that prevented the physiochemical degradation of the electrochemically active materials due to the high temperature exposure and preserved the full electrical functionality.

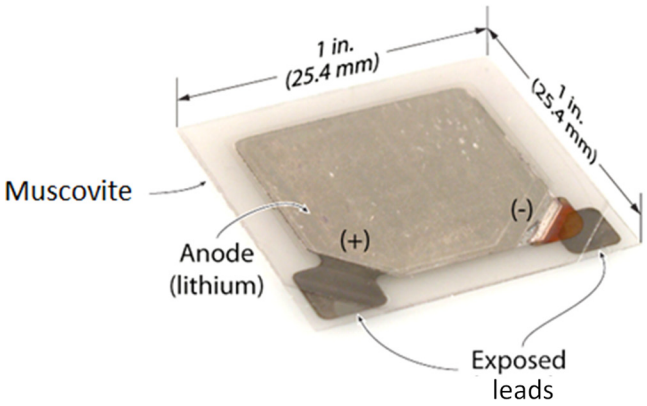

Figure 2. *Perspective photo of all-solid state thin film Li-ion battery with dimensions. Manufactured by FrontEdge Technology Inc.*

The multifunctioinal design of the battery packaging to achieve integrity of the electrochemical cell as well as efficient structural capability has never been investigated. Such a design is an enabling technology for the structural battery concept. The preliminary step is to characterize the stress-strain field and the electromechanical failure modes of the TFB-CFRP laminate under loading. Whether the TFB is embedded within the CFRP sub-laminate, Figure 4(a), or externally bonded onto its surface, Figure 4(b), a three-dimensional stress-strain field has to be considered because of the lay-up transition at the battery ends, as well as of the highly inhomogeneous mechanical properties of the material layers involved. Applicable failure modes include ply failure, disbonding, mixed-mode delamination at multiple bi-material interfaces and delamination buckling. Any of these mechani-

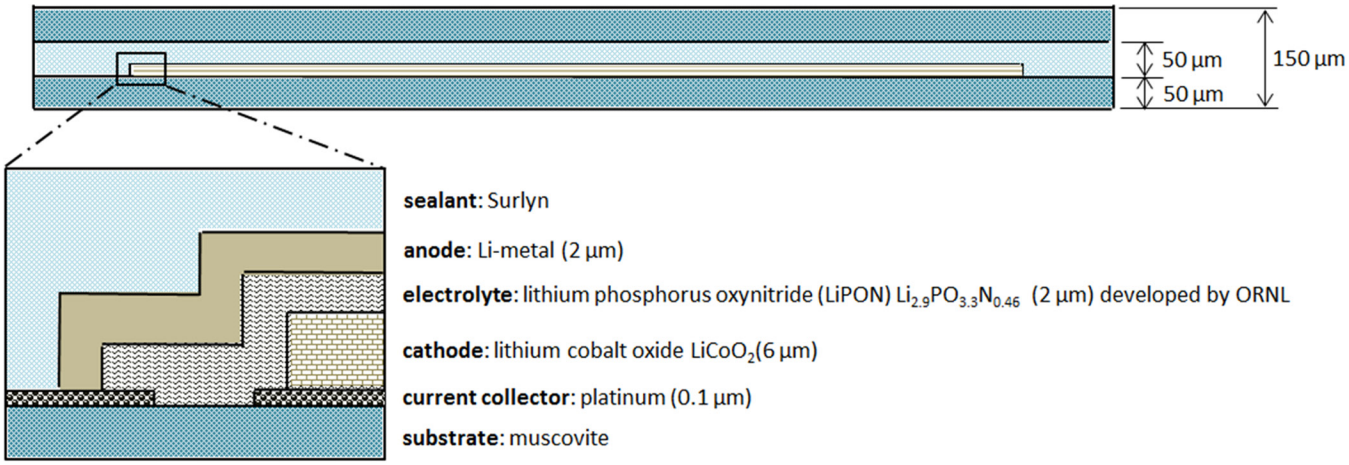

Figure 3. *Cross-sectional schematic of the commercially available TFB showed in Figure 2.*

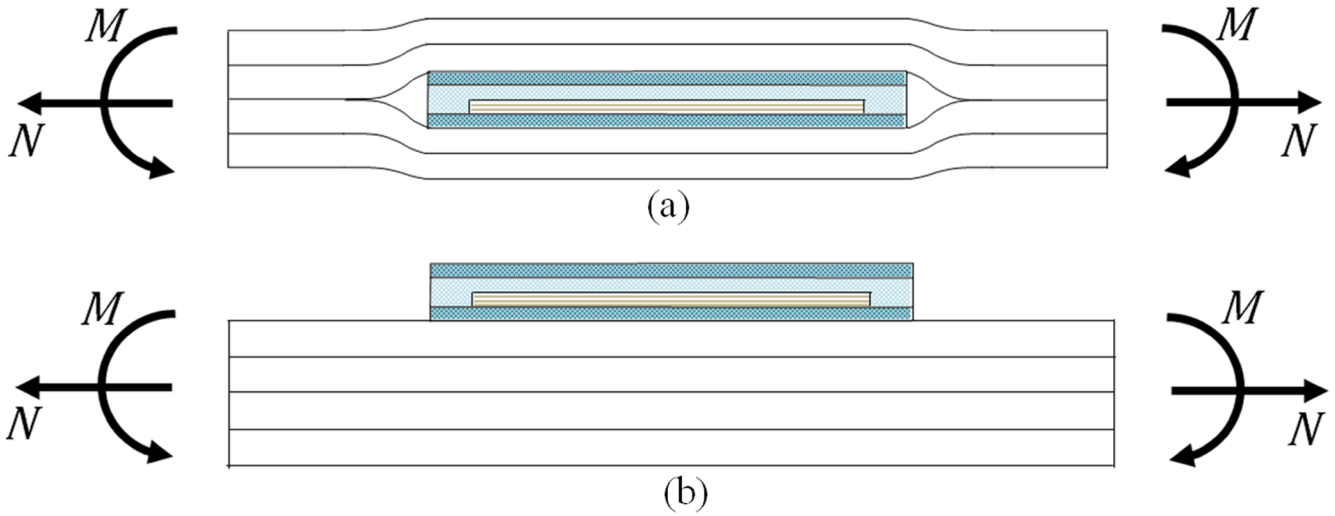

Figure 4. *Hybrid thin film lithium ion-graphite composite battery (TFB-CFRP) laminate configurations: thin film battery (a) embedded within the carbon fiber /epoxy laminate, or (b) bonded onto the laminate surface.*

cal failures can lead to the electrical failure by introducing an electrical discontinuity, an electrical short or a path for air and moisture through the battery packaging, leading to contamination of the electrochemically active materials.

Research conducted in [22,23] showed that the aforementioned commercial TFB was capable to operate up to a radius of curvature of 181 mm [22] and under out-of-plane pressures as high as 830 kPa [23] without any detrimental effects on the electrochemical performance. The same TFB type was successfully embedded in a CFRP laminate and electrochemically characterized under uniaxial mechanical tension. The study focused on the laminate residual mechanical strength and stiffness, which was not penalized by the presence of the TFB embedded at the laminate mid-plane. On the other hand the TFB electrical failure, which consisted of an irreversible and complete loss of capacity, occurred prematurely at about 50% of the laminate mechanical failure strain [24,25]. These electromechanical tests proved that the mechanical boundary conditions have no effect on the electrochemical performance up to a sudden electrical failure. This was confirmed by the multi-physics finite element analysis developed by [21]. The finding implies that the sudden electrical failure is caused by a mechanical failure, such as the failure of the packaging layers, with subsequent cell contamination or tearing, or by cracking of the electrodes or the electrolyte.

To date, neither the stress-strain field nor the mechanical failure modes have been characterized for basic loading conditions. This fundamental knowledge is required in order to prove the functionality and assess the benefits of an optimized TFB-CFRP system, which includes a battery packaging specifically designed for this multifunctional application. Unlike standard flexible electronics, the packaging has to be physically and chemically compatible with the TFB deposition and annealing process, as well as highly performing in terms of specific modulus and specific strength, and capable of ensuring sealing integrity when subjected to severe stress.

Taking advantage of the highest specific energy on the market, currently available TFBs used as structural elements could theoretically reduce the weight of certain aircraft types even without relying on load bearing electrodes, provided that the packaging possesses mechanical properties comparable to airframe structural materials. Hence the structural efficiency of substrate and sealant becomes a determining factor of success.

In order to clarify the concept we analyzed the weight reduction obtained by replacing the energy storage system of a propeller aircraft with a structural TFB system. The weight of the original propulsion system, based on an electric engine or an internal combustion engine, is assumed to be the same as an equivalent electric propulsion system. It is important to note that this assumption is applicable to reciprocating and small turbine engines, but it is not valid for turbofan cores, which have a higher energy density than any currently available electric motor [26]. The new aircraft weight W^* is given by

$$W^* = W - W_{F/B} + W_{TFB} \tag{1}$$

where W is the original gross weight at takeoff, $W_{F/B}$ is the weight of the fuel W_F or of the original batteries W_B and W_{TFB} is the weight of the TFB active components required to power the aircraft. For preliminary calculation purposes, it is assumed that the packaging has the same specific strength and specific modulus as the airframe materials being replaced. This permits omitting its weight from the above equation.

The new battery weight W_{TFB} is equal to the total propulsion energy required for the new aircraft configuration to complete a mission, E_S^*, divided by the product of the TFB energy density, e, and the efficiency of the new electric mo-

tor, η_M. The new mission energy, E_S^* is therefore defined as the energy delivered by the engine and is equivalent to the total drag of the new configuration multiplied by the flight range and divided by the propeller efficiency. For an electric aircraft, E_S^* is related to the total mission energy of the original configuration E_S as follows

$$E_S^* = E_S \frac{W^*}{W} \tag{2}$$

The above equation can be derived by assuming that the mission is comprised of a steady level flight only, and that cruise speed, aerodynamic efficiency and propeller efficiency of the new configuration are equal to the original configuration. Through algebraic substitution we obtain

$$\frac{W^*}{W} = \frac{1-\frac{W_B}{W}}{1-\frac{E_S}{e\eta_M}} \tag{3}$$

For an aircraft equipped with an internal combustion engine a similar equation can be derived with the additional assumptions that the rate of fuel consumption and the aerodynamic efficiency remain constant throughout the flight

$$\frac{W^*}{W} = \frac{1-\frac{W_B}{W}}{1-\frac{E_S}{e\eta_M}\frac{W}{W-W_F/2}} \tag{4}$$

Empirical data from different aircraft categories were averaged in order to calculate the nondimensional groups of aircraft weights in Equations (3) and (4). The data are summarized in Table 1. The electric motor efficiency, η_M, was assumed equal to 0.95. To calculate the mission energy, E_S, the original flat rated engine power was multiplied by the maximum range and divided by the cruise speed, thereby neglecting takeoff and landing. The resulting semi-empirical curves for the weight change ratio are plotted in Figure 5 at increasing TFB energy densities, starting from the today's available energy density of 353 Wh/kg. The white plot area identifies the aircraft configurations that benefit from weight saving. The grey plot area indicates weight increase. The model shows that weight saving could be currently achieved for electric aircraft such as High Altitude Long Endurance (HALE), mini-UAV and motor gliders. For aircraft characterized by higher mission energy per unit mass, such as UAVs with internal combustion engines and general aviation, further improvement in specific energy is required. However, a battery packaging with the assumed structural efficiency is not technology ready and its mechanical performance requirements have to be assessed.

Table 1. Aircraft Weight and Power Plant Energy Characteristics Utilized to Feed the Semi-empirical Weight Prediction Model Shown in Figure 5.

Aircraft	E_S [kWh]	W [kg]	$W_{F/B}$ [kg]	E_S/W [kWh/kg]
Pipistrel Taurus Electro G2[1]	7.17	472.50	101.00	0.015
NASA Helios[2,3]	21.00	929.00	148.75	0.023
AeroVironment RQ-11 Raven[4]	0.11	1.90	0.46	0.056
Solar Impulse[5]	120.00	2000.00	450.00	0.060
AAI RQ-7A Shadow[4]	34.25	154.00	23.10	0.222
AAI Shadow 400[4]	73.47	201.00	68.40	0.366
Cessna 172R[5]	565.51	1111.00	144.00	0.509
General Atomics RQ-1 Predator[4]	7680.4	1020.00	295.00	0.753
Pilatus PC-12[5]	4187.09	4740.00	1226.00	0.883
Piaggio P-180[5]	5291.84	5488.00	1271.00	0.964

[1]http://www.pipistrel.si/plane/taurus-electro/technical-data.
[2]http://www.nasa.gov/centers/dryden/news/FactSheets/FS-068-DFRC.html.
[3]Saft LO 26 SHX battery data sheet.
[4]Jane's Unmanned Aerial Vehicles and Targets, Issue thirty, May 2008.
[5]Jane's All the World's Aircraft 2010–2011.

The objective of this paper is to introduce the concept of hybrid TFB-CFRP laminate and to experimentally characterize the stress-strain field and failure mechanism of the multifunctional laminate subjected to uniaxial strain, single curvature and a combination of the two. This work is intended to support the future development of damage initiation and propagation analyses finalized to the optimization of the TFB packaging design. In this perspective, experimental data was required for determining the critical failure modes to be considered and for validating such analysis methods. The research also aims at providing a performance envelope for the current TFB technology that could be used as a baseline for the next generation of airborne thin film structural batteries.

2. METHODOLOGY

A commercially available TFB was utilized to manufacture TFB-CFRP laminates. The chemistry of the selected battery, as well as its manufacturing process, is representative of the commercial state-of-the-art that is currently adopted by all the manufacturers of solid state thin film lithium-ion batteries. The TFB selected for this study, Figure 2, was deemed the most suitable for this application because of the simplicity of the three-layer design and high stiffness of the packaging. Two laminate configurations were considered. The first was comprised of a TFB embedded at the laminate mid-plane and co-bonded within the CFRP sub-laminate, Figure 4(a). The second was the secondary bonding of the TFB onto the surface of a pre-cured CFRP sub-laminate, Figure 4(b).

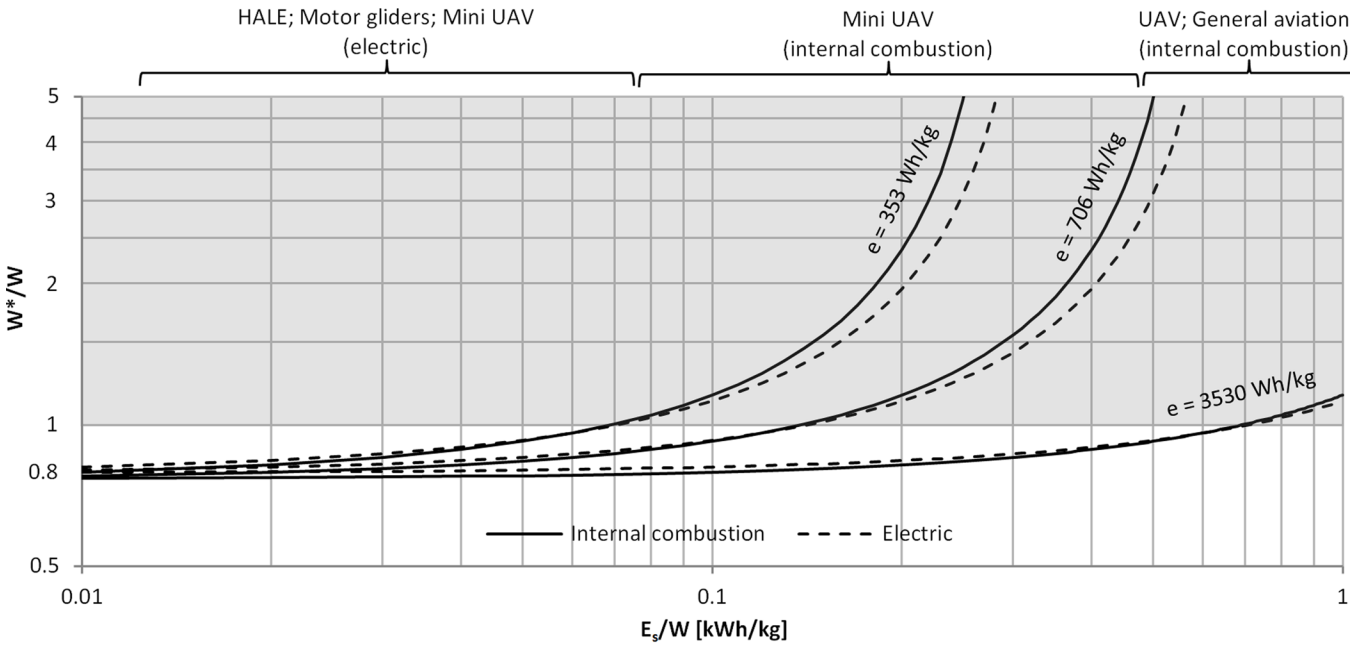

Figure 5. *Predicted gross weight of aircraft equipped with TFB energy storage system (W*) normalized by the original gross weight at takeoff (W), plotted as a function of the original specific mission energy. Semi-empirical curves [as per Equations (3) and (4) and averaged data from Table 1] plotted at increasing TFB specific energies (e).*

Mechanical tests were conducted in order to measure the stress-strain field under uniaxial loading and assess the applicability of classical analysis methods in mechanics of composite materials. Disbonding, delamination characteristics and laminate mechanical failure modes were also assessed in order determine the weakest link and critical properties that lead to mechanical failure. The cyclic TFB thickness variation due to the migration of the lithium ions during battery charge and discharge, which could generate interlaminar normal stress in the laminate, was also experimentally measured. Finally, an electrochemical characterization under mechanical loading was performed in order to determine the strain and curvature at electrical failure.

2.1. Materials

The TFBs utilized in this research are manufactured by FrontEdge Technology under license from the Oak Ridge National Laboratory (ORNL), Figure 2. Chemistry and thicknesses of the cell components are summarized in Figure 3. The active components are encased by two 50 μm thick muscovite substrates bound by a thermoplastic layer of Surlyn sealant, leading to a total thickness of 150 μm. The battery is a 25.4 mm square with a nominal voltage of 4.2V, and a nominal capacity of 1 mAh. The energy density measured by the authors with respect to the mass of active components is 353 Wh/kg, which drops to 22 Wh/kg with packaging weight included. Experimental characterizations of the same battery under mechanical loading were performed by [22–25].

The electrochemically active components of the battery are grown by a sequence of different physical vapor deposition (PVD) processes performed in-situ on the substrate. The need of annealing the cathode at temperatures of 300°C or higher to increase the ionic conductivity requires dimensional stability of the substrate material at those temperatures in order to avoid cracking, disbonding or undesired crystalline orientation of the cathode due to thermal stresses. Chemical stability is also important in order to avoid releasing contaminants in the controlled atmosphere of the deposition chamber. All these requirements have to be considered for the selection of a substrate material. The manufacturing process was discussed in detail in [27–31].

The active components are highly reactive with N_2 [27], O_2 [28] and H_2O [32], therefore the TFB has to be hermetically sealed. A failure of the sealant or substrate during manufacturing or operation of the TFB-CFRP leads to the failure of the battery by compromising its ability to store energy. The electrical capacity loss can be almost instantaneous or can fade progressively, depending on the flow rate of contaminants entering the battery. Since the CFRP material is hygroscopic, this failure mode applies to the embedded TFB configuration as well.

Mechanical properties of muscovite and Surlyn are listed in Table 2. The first is a crystalline mineral whose crystallographic structure is comprised of 1 nm thick layers separated by perfect basal cleavages. This characteristic determines low fracture toughness against cracks that are planar with the battery. On the other hand it can be considered quasi-isotropic in the battery plane [33] with an elastic modulus

Table 2. Relevant Mechanical Properties of Materials.

Property	Symbol	Muscovite[1]	Surlyn	IM7/977-3[2]	AF 163-2[3]
Tensile modulus of elasticity [GPa]	E_1	178[4]	0.28[5]	162	1.10
	E_2	178[4]	0.28[5]	8.34	1.10
Shear modulus of elasticity [GPa]	G_{12}	70.7[4]	0.11[6]	4.96	0.41
Poisson's ratio	v_{12}	0.26[7]	0.3[8]	0.34	0.34
Strain to tension failure [%]	ε_1^{TU}	unkn.	8.00[5]	1.46	unkn.
Mode I fracture toughness [J/m^2]	ε_2^{TU}	unkn.	8.00[5]	0.77	unkn.
	G_{IC}	1.30[9]	1200[10]	316	3682

[1]Average in-plane properties in the plane parallel to the basal cleavage, which coincides with the battery plane.
[2]Cytec IM7/977-3 data sheet.
[3]3M Scotch-Weld Structural Adhesive Film AF 163-2 data sheet.
[4]McNeil *et al.*, *J Phys.: Condens. Matter* 5, 1681 (1993).
[5]Yield strain, ref. NCAR Report FRB-4 (1965).
[6]Calculated assuming isotropy and ? = 0.3.
[7]Calculated assuming isotropy in the battery plane.
[8]Assumed.
[9]Hill *et al.*, *Int. J. Fracture* 119/120, 365 (2003).
[10]Compston *et al.*, *J Mater. Sci. lett.* 20, 509 (2001).

of 178 GPa, which is in the range of intermediate modulus CFRP materials. Surlyn is a high toughness thermoplastic polymer with a melting temperature of 98°C. A compatibility study to the composite curing process revealed that in some batteries the Surlyn layer is affected by long strands of bubbles along the edges of the active components, and that during curing of the TFB-CFRP laminate bubbles diffused within the sealant layer and coalesced into a disbonded front, Figure 6. These defects could potentially cause delamination onset within the battery packaging, Figure 7.

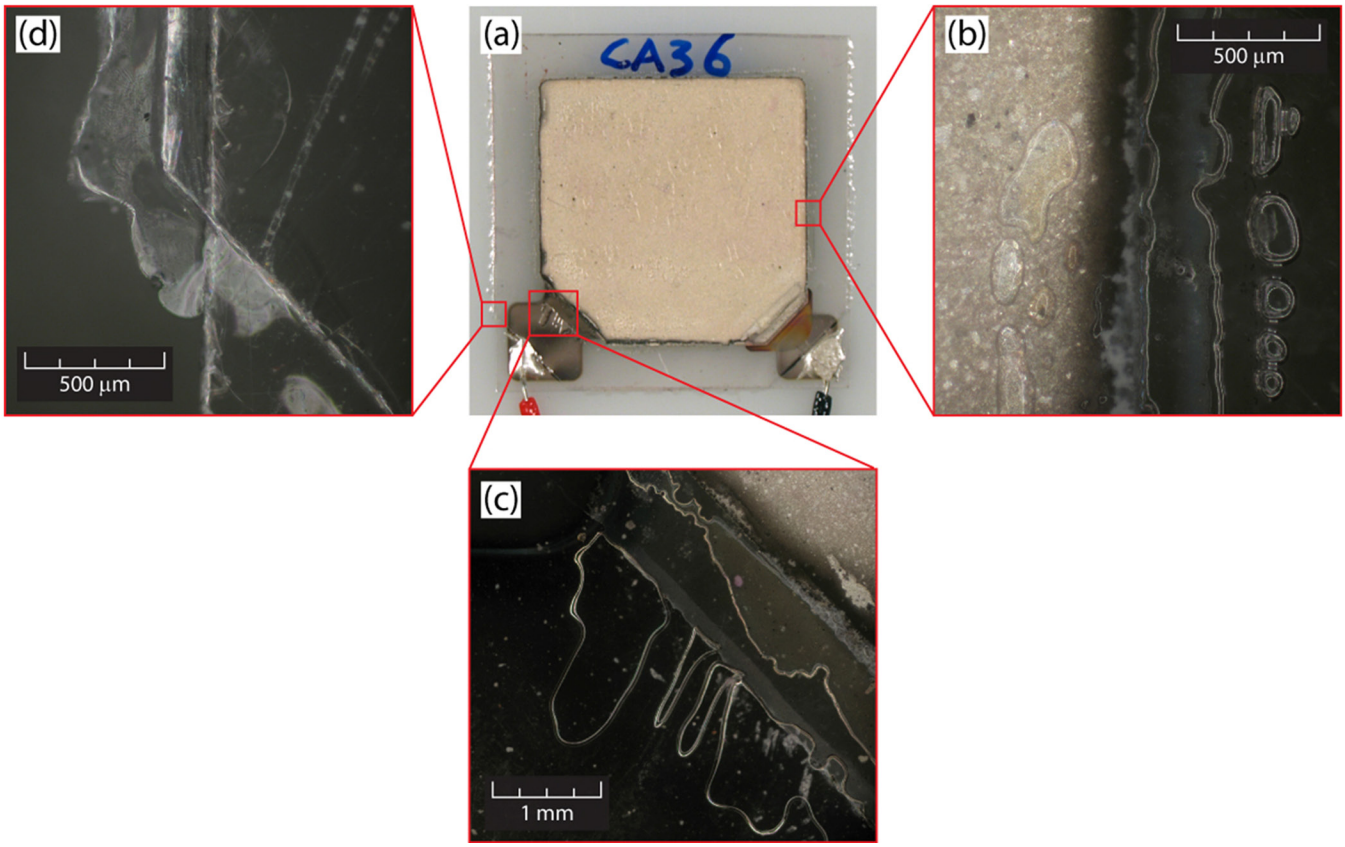

Figure 6. *Micrographs of a TFB after processing at 121°C for one hour under vacuum bag (–711 mmHg) showing sealant bubbling and a disbonded front along the edge of the active components.*

Figure 7. *Cross-sectional schematic of the TFB with locations of disbonded areas, as shown in Figure 6, highlighted with dotted lines.*

The TFB-CFRP laminates were cured by heated press molding of IM7/977-3 prepreg tape materials at 132°C and 590 kPa, with a cure time of two hours. In the case of embedded TFB, the battery was laminated within the prepreg material prior to curing and without the addition of adhesive film (AF). For the externally bonded TFB configuration, the CFRP laminate was pre-cured with the same process and the battery was subsequently bonded using one layer of epoxy adhesive film 3M AF163-2 cured for 1.5 hours at 121°C in the vacuum bag. These cure cycles were validated by the authors in order to retain the full functionality of the battery. The mechanical properties for the carbon/epoxy material and the adhesive film are listed in Table 2.

For the electromechanical characterization of the TFB-CFRP laminate, the battery was connected to the testing circuit through flat flexible cables (FFC), Nicomatic 254PW01E6095 polyester coated single copper conductor. The FFCs weree 0.25 mm thick and 5.12 mm wide. They were connected to the TFB leads using MG Chemicals silver conductive epoxy 8331-14G. For the embedded battery configuration they were laminated within the CFRP at the laminate mid-plane.

Unlike previous studies [24,25], the battery was not encased within a pre-cured polymeric case, but silicone conformal coating MG Chemicals 422-55 was applied on the exposed leads only, Figure 2, to insulate the connections and prevent electrical shorting with carbon fibers.

2.2. Experimental

The experimental campaign was comprised of five test types: double cantilever beam (DCB); uniaxial mechanical tension; battery thickness variation occurring during charge/discharge cycling; uniaxial mechanical tension with battery capacity monitoring and four point bending with battery capacity monitoring, Table 3 The battery thickness variation test setup and procedure were conceived ad hoc since a test standard is not available. The remaining tests adopted ASTM standard methods for reinforced plastics modified to cope with the multifunctional system.

The specimens for DCB test were 25.4 mm wide, which is equal to the TFB width, and 304.8 mm long. Tests were conducted according to the ASTM standard [34]. Three baseline specimens, comprised of thirty plies oriented at 0° for a laminate thickness of 3.8 mm, were tested to determine the mode I fracture toughness G_{IC} of the CFRP material. Three additional specimens with a TFB embedded at the laminate mid-plane were then tested. These specimens featured a battery embedded at specimen mid-span, leading to the staking sequence (0_{30}) away from the battery and (0_{15}/TFB/0_{15}) at battery location. The crack was started from the loaded end of the specimen, at the laminate mid-plane, and propagated towards the TFB. A precrack was induced so that a delamination was visually observed on the edge of the specimen before staring the test. The objective was to determine the G_{IC} and the crack propagation path. The G_{IC} was calculated by dividing the total strain energy released during the test by the final crack surface measured from the tip of the precrack.

Uniaxial mechanical tension tests with full-field strain monitoring were performed in order to characterize the stress-strain field for different laminate lay-ups. The procedure complies with the standard ASTM test [35], except for an increased specimen width of 76.2 mm, Figure 8. This modification was introduced to minimize the interaction between the edge effect and the stress-strain gradient caused by the TFB, which was located at the center of the speci-

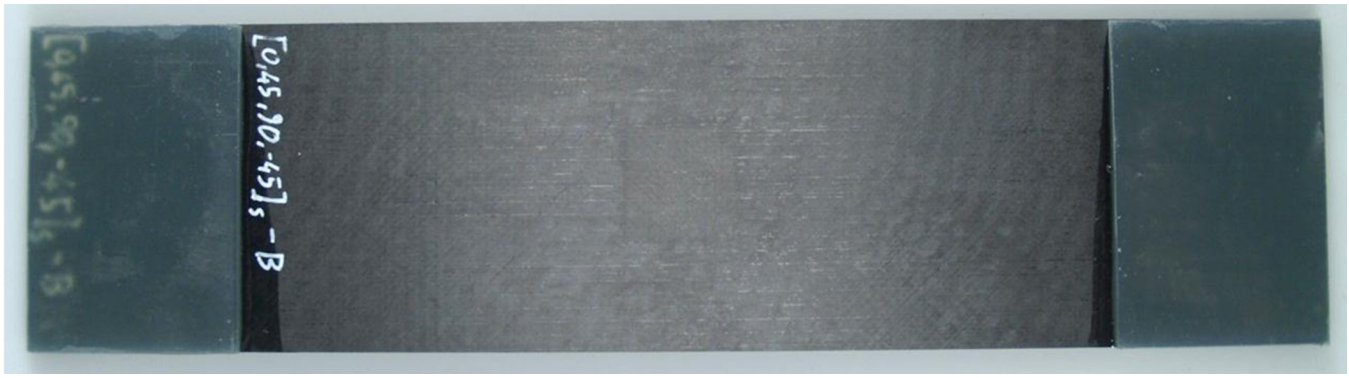

Figure 8. *Uniaxial mechanical tension test specimen with embedded TFB at laminate mid-plane. Laminate stacking sequence is (0/45/90/–45/TFB/–45/90/45/0).*

Table 3. Summary of Tests.

Test Description	Lay-ups	Repetitions
Double cantilever beam (DCB)	(0_{30})	3
	$(0_{15}/TFB/0_{15})$	3
Uniaxial mechanical tension with full-field strain monitoring	(0/90/TFB/90/0)	1
	$(0_2/TFB/0_2)$	1
	(0/45/90/–45/TFB/–45/90/45/0)	1
	$[(0/45/90/–45)_S/AF/TFB]$	1
	$(0_8/AF/TFB)$	1
TFB thickness variation during charge/discharge cycling	TFB alone	1
Uniaxial mechanical tension with TFB capacity monitoring	[0/45/90/–45/TFB/–45/90/45/0]	2
Four point bending with TFB capacity monitoring	$[(0/45/90/–45)_3/TFB/(–45/90/45/0)_3]$	2
	$[(0/45/90/–45)_{3S}/AF/TFB]$	2
	$[TFB/AF/(–45/90/45/0)_{3S}]$	2

men. A total of three lay-ups with embedded battery were investigated: a 4-ply cross-ply laminate, a 4-ply unidirectional laminate tested along the 0° direction and an 8-ply quasi-isotropic laminate. The embedding method adopted throughout this study is referred to as interlaminar embedding, since it consisted of enclosing the battery in the space between two plies, as opposed to enclosing it into a ply cut-out. This design avoided sharp stress-strain gradients to arise at the battery edges, although it led to resin pockets at the TFB ends, Figure 9. The applied strain was increased only up to a far-field strain of approximately 3000 µstrain in order to observe the elastic behavior. The failure behavior for this laminate configuration was already reported in [24,25].

Two additional 8-ply lay-ups with an externally bonded TFB were tested in uniaxial tension: a unidirectional laminate tested along the 0° direction and a quasi-isotropic laminate. Their stacking sequences at battery location were $(0_8/AF/TFB)$ and $[(0/45/90/–45)_S/AF/TFB]$ respectively. A specimen with an externally bonded battery is shown in Figure 10. The test procedure was the same as for the embedded TFB configuration, but the applied load was increased up to failure in order to investigate the elastic stress-strain field as well as the failure mode.

For all the uniaxial mechanical tension tests a digital image correlation (DIC) technique was adopted to monitor the surface strain of the specimen. To avoid using FFCs that would alter the strain field or interfere with the optical measurement technique, the electrical response of the TFB-CFRP laminate under loading was investigated separately.

Contrary to the common perception that their thickness remains constant, the lithium ion batteries expand during charge and contract during discharge. This thickness, thus

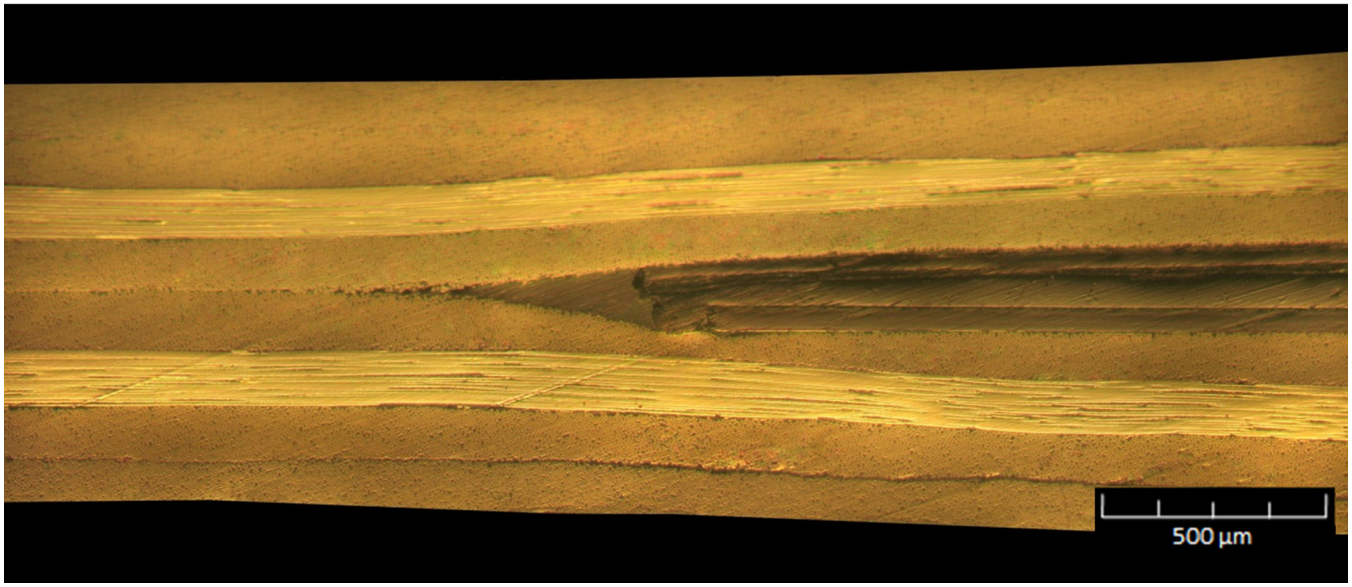

Figure 9. *Micrograph of quasi-isotropic laminate with TFB embedded at laminate mid-plane. Laminate stacking sequence is (0/45/90/–45/TFB/–45/90/45/0).*

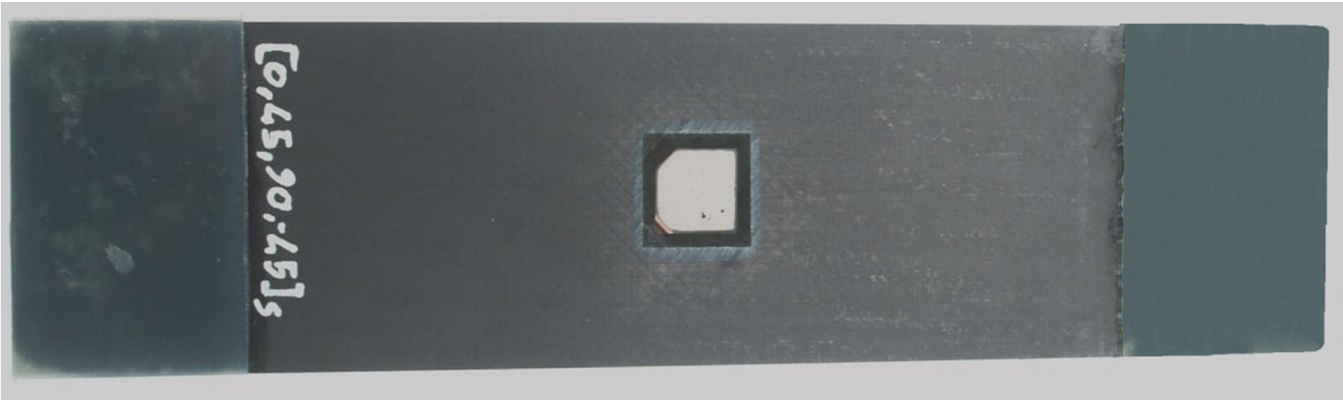

Figure 10. *Uniaxial mechanical tension specimen with externally bonded TFB. Laminate stacking sequence at battery is* $[(0/45/90/-45)_S/AF/TFB]$.

volume, change is caused by lithium ion intercalation into host electrode materials. Since the TFB has a metallic lithium anode instead of an intercalation compound, the thickness increase is attributed to the plating of lithium at the anode during the charging process. The DIC was employed for monitoring the thickness increase of one TFB alone during a full electric charge process. A full charge/discharge cycle was performed before the test in order to condition the battery. Discharge was operated under a constant resistive load of 3.8 kΩ, which led to an average discharge rate of 1C (i.e. 1 ma discharge current). Charge took place at a constant voltage of 4.2 V. The battery was considered fully discharged when the voltage reached 3 V, the lower limit to avoid overdischarge, while full charge was reached when the current dropped below 50 μA. The DIC measured the out-of-plane displacement of the TFB outer surface at anode side with time intervals of 2 minutes, starting from the fully discharged state, which was taken as the reference state. Therefore the displacement field corresponding to the fully charged state was equal to the maximum thickness increase. The TFB temperature was monitored for the entire duration of the test with an infrared (IR) camera with ±1°C accuracy.

Lastly, an electrochemical characterization of the TFB-CFRP laminate subjected to uniaxial tension and flexure was conducted. The purpose was to assess the operational envelope and to determine the interaction between electrical and mechanical failure modes, where electrical failure was the partial or total capacity loss. Two specimens with a stacking sequence (0/45/90/–45/TFB/–45/90/45/0) were tested up to failure through uniaxial mechanical tension. The selected laminate lay-up showed the best correlation between experimentally measured and calculated strain field in the mechanical tests, thereby increasing the degree of confidence for the calculation of the strain at failure. The dimensions of the specimens matched those of the previously described mechanical tension tests, but in this case FFCs were connected to the battery and laminated within the CFRP plies. Figure 11 shows the cables exiting from the laminate and connecting to the charge/discharge circuit (not shown) to allow for capacity monitoring. The discharge or charge capacity was calculated by numerically integrating the discharge or charge current over time. The procedure and characteristics of the charge and discharge circuit were as previously described.

For the mechanical tension tests with capacity monitoring, constant strain intervals of increasing magnitude were applied until failure, where the duration of an interval corresponded to the time required to perform a full discharge followed by a full charge for capacity measurement under

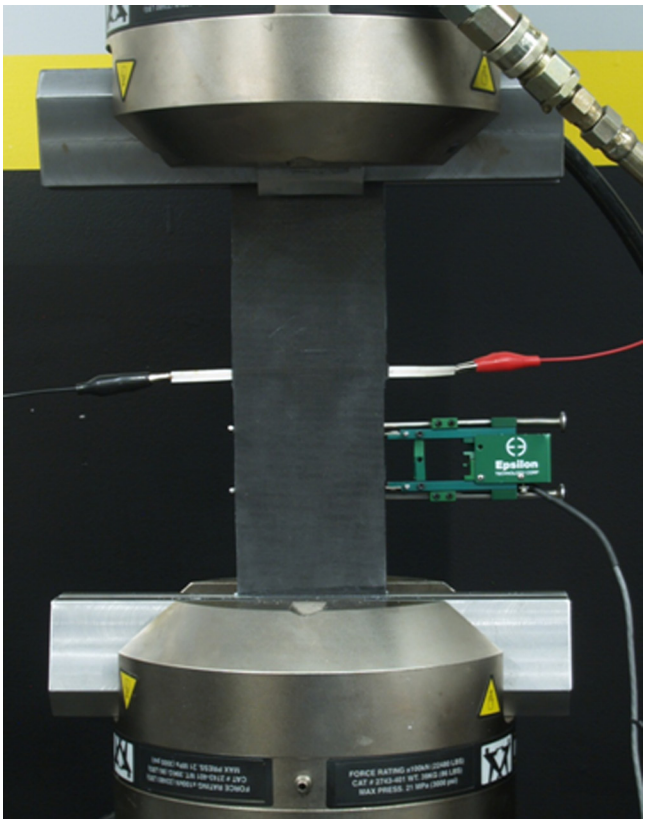

Figure 11. *Electromechanical uniaxial tension test setup showing the hybrid TFB/graphite laminate specimen clamped by the grips of test frame. Laminate stacking sequence is (0/45/90/–45/TFB/–45/90/45/0).*

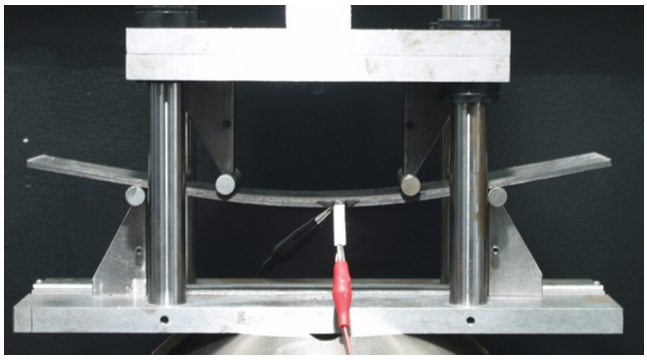

Figure 12. *Electromechanical flexure test setup with standard 60:1 span to thickness ratio, showing the hybrid TFB/graphite laminate specimen loaded by the four point bending fixture. Laminate stacking sequence is* $[(0/45/90/–45)_3/TFB/(–45/90/45/0)_3]$.

constant strain. Load was released after each strain interval and capacity was measured again at zero strain. The far-field strain was measured by an extensometer, Figure 11, for control and data acquisition, while the strain at failure location was calculated using the analysis methods described in the following section.

Similarly, four point bending tests were conducted on laminates with embedded or externally bonded battery configurations, Figure 12. While in the first configuration the TFB was subjected to pure curvature, the second led to curvature and compressive or tensile in-plane strain depending on which side of the specimen the TFB was bonded on. The width of the specimen was always 76.2 mm, while the support span to thickness ratio was initially set to 60:1 with a support span of 180 mm and a loading span of 90 mm. The laminate stacking sequences were $[(0/45/90/–45)_3/TFB/(–45/90/45/0)_3]$, $[(0/45/90/–45)_{3S}/AF/TFB]$ and $[TFB/AF/(–45/90/45/0)_{3S}]$. For the embedded battery configuration, a stacking sequence (0/90/TFB/90/0) was also tested with an increased span-to-thickness ratio of 145:1. Support and loading span were 72.5 mm and 36.5 mm respectively. This modified setup, which does not comply with the ASTM standard [36], was designed for applying higher curvatures to the battery without experiencing mechanical failure of the laminate. The same load-hold load-unload procedure with increasing curvature intervals was adopted, but in this case the test was conducted under displacement control. The curvature applied by a given displacement of the test frame was calculated through integration of the elastic line equation. Small deformations, normality condition of the sections and uniform bending stiffness were assumed. The uniformity of the bending stiffness is applicable only if the presence of the battery does not significantly change the section inertia of the CFRP laminate. The far-field strain applied to the battery was then calculated by multiplying the curvature by half the CFRP laminate thickness. The curvature is reported in the results section as the radius of curvature, which was assumed equal to the inverse of the curvature.

2.3. Analysis

Classical laminate theory (CLT), finite element analysis (FEA) and a closed form elasticity solution of the TFB-CFRP laminate were utilized to interpret the experimental results and calculate the strain at failure. These methods were validated by comparing their results with the experimentally measured elastic strain field from the uniaxial mechanical tension tests. Given the applied far-field strain ε_0, the strain field at the center of the specimen, which was affected by the presence of the TFB, was calculated and compared to the surface strain field measured by the DIC.

The first analysis method used CLT to calculate the apparent modulus of elasticity in the x-direction at a point away from the battery, where the laminate was comprised of the CFRP layers only, and at the battery location. The model accounted for the stiffness of the battery substrate, sealant and the adhesive film. The x-direction was defined as the loading direction. The laminate strain at the battery was then calculated by multiplying the far-field strain by the ratio of the two moduli multiplied by their respective thicknesses. The results obtained with this method are identified in the results section with the acronym CLT.

At specimen mid-span, the section was not constant across the width due to the presence of the battery. In order to account for the resulting stress redistribution, which was ignored by the first analysis method, a second analysis method that employs a linear finite element solution with NX Nastran SOL101 was developed. FEA also accounted for the extension-bending coupling caused by the laminate asymmetry. The entire specimen was modeled with linear shell elements (CQUAD4) and a mesh size of 1.524 mm that matched the DIC resolution. The element formulation used the CLT for computing element stiffness and outputs, therefore plane stress and uniform strain through-the-thickness were assumed. The desired far-field strain was applied by an enforced nodal displacement at the loaded end. The transverse strain was unconstrained.

The third analysis method was a linear elastic shear lag model that was developed in order to capture the extensive three-dimensional stress-strain field of the externally bonded battery configuration. The sealant, identified by the letter *s*, and the adhesive film, identified by *af*, were assumed to carry only shear, while the bending and shearing deformation of the upper and lower substrates, *su* and *sl* respectively, were neglected. The carbon/epoxy composite material was modeled as an equivalent isotropic material with the apparent laminate Young's modulus in the x-direction calculated according to the CLT. Bending and shearing deformation of the CFRP were also neglected. Perfect bonding was assumed at all interfaces and the presence of the active components was neglected due to their relatively small thickness. Based on these assumptions, when a far-field stress σ_0 is applied to the CFRP laminate, a normal stress σ_x is generated in the

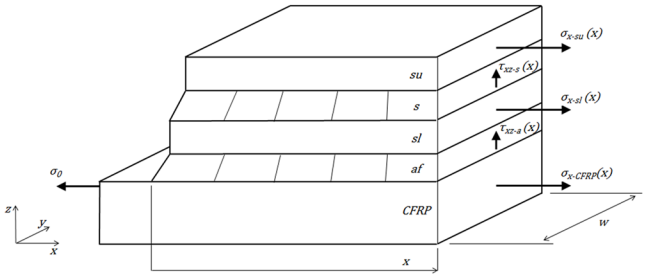

Figure 13. *Shear lag elasticity model of the externally bonded TFB, stress representation. Laminate layers are: carbon/epoxy sub-laminate (CFRP); adhesive film (a); lower substrate (sl); sealant (s); upper substrate (su).*

CFRP, *su* and *sl* layers, and a shear stress τ_{xz} is carried by the *a* and *s* layers, Figure 13. No other stress components arise, therefore the equilibrium equations are reduced to three, one for each of the layers that carries axial loading. The addition of the strain-displacement and stress-strain equations leads to a system of thirteen equations with thirteen unknowns.

The resulting governing equations are

$$\begin{cases} \dfrac{d^2\sigma_{x-su}}{dx^2} - \lambda_1^2\sigma_{x-su} - \beta_1\sigma_{x-CFRP} + C_1 = 0 \\ \dfrac{d^2\sigma_{x-CFRP}}{dx^2} - \lambda_2^2\sigma_{x-CFRP} - \beta_2\sigma_{x-su} + C_2 = 0 \end{cases} \tag{5}$$

where the known parameters are conveniently grouped as follows

$$\begin{aligned} \lambda_1^2 &= \frac{G_s}{t_s}\left(\frac{1}{t_{su}E_{su}} + \frac{1}{t_{sl}E_{sl}}\right) \\ \beta_1 &= \frac{t_{CFRP}G_s}{t_{su}t_{sl}t_sE_{sl}} \\ C_1 &= \sigma_0\frac{t_{CFRP}G_s}{t_{su}t_{sl}t_sE_{sl}} \\ \lambda_2^2 &= \frac{G_{af}}{t_{af}}\left(\frac{1}{t_{sl}E_{sl}} + \frac{1}{t_{CFRP}E_{CFRP}}\right) \\ \beta_2 &= \frac{t_{su}G_{af}}{t_{sl}t_{CFRP}t_{af}E_{sl}} \\ C_2 &= \sigma_0\frac{G_{af}}{t_{sl}t_{af}E_{sl}} \end{aligned} \tag{6}$$

In the above definitions *t*, *E* and *G* identify thickness, Young's modulus and shear modulus of elasticity.

Equation (3) is a system of coupled second-order linear ordinary differential equations, whose general solutions are

$$\sigma_{x-su}(x) = B_1\cosh(A_1x) + B_2\sinh(A_1x) + B_3\cosh(A_2x) + B_4\sinh(A_2x) \tag{7}$$

$$\begin{aligned} \sigma_{x-CFRP}(x) = \frac{1}{B_1}[&(A_1^2-\lambda_1^2)B_1\cosh(A_1x) \\ &+(A_1^2-\lambda_1^2)B_2\sinh(A_1x) + (A_2^2-\lambda_1^2)B_3\cosh(A_2x) \\ &+(A_2^2-\lambda_1^2)B_4\sinh(A_2x) - \lambda_1^2C + C_1] \end{aligned} \tag{8}$$

The known parameters A_1 and A_2 are defined as

$$\begin{aligned} A_1 &= \sqrt{\frac{1}{2}\left[\lambda_1^2 + \lambda_2^2 + \sqrt{(\lambda_1^2-\lambda_2^2)^2 + 4\beta_1\beta_2}\right]} \\ A_2 &= \sqrt{\frac{1}{2}\left[\lambda_1^2 + \lambda_2^2 - \sqrt{(\lambda_1^2-\lambda_2^2)^2 + 4\beta_1\beta_2}\right]} \\ C &= \frac{\lambda_2^2C_1 - \beta_1C_2}{\lambda_2^2\lambda_1^2 - \beta_1\beta_2} \end{aligned} \tag{9}$$

The terms B_1 to B_4 were calculated for the following boundary conditions

$$\begin{aligned} x = 0 \rightarrow \sigma_{x-su} = 0;\ \ \sigma_{x-CFRP} = \sigma_0 \\ x = l \rightarrow \sigma_{x-su} = 0;\ \ \sigma_{x-CFRP} = \sigma_0 \end{aligned} \tag{10}$$

leading to

$$\begin{aligned} B_1 &= \frac{-A_2^2C + C_1 - \sigma_0\beta_1}{A_2^2 - A_1^2} \\ B_2 &= \left(\frac{A_2^2C - C_1 + \sigma_0\beta_1}{A_2^2 - A_1^2}\right)\frac{\cosh(A_1l) - 1}{\sinh(A_1l)} \\ B_3 &= \frac{A_1^2C - C_1 - \sigma_0\beta_1}{A_2^2 - A_1^2} \\ B_4 &= \left(\frac{A_1^2C - C_1 + \sigma_0\beta_1}{A_2^2 - A_1^2}\right)\frac{1 - \cosh(A_2l)}{\sinh(A_2l)} \end{aligned} \tag{11}$$

All the other unknowns of the system, such as the remaining stresses, strains and displacements, were then solved by algebraic substitution.

The results provided in the next section are based on the actual thicknesses taken from microscopies of polished specimen sections, similar to the micrograph shown in Figure 9. The following thicknesses were used: 0.125 mm for the CFRP plies; 0.06 mm for the TFB substrates; 0.08 mm for the TFB sealant and 0.09 mm for the adhesive film.

3. RESULTS

Typical load displacement plots for the DCB tests are shown in Figure 14. The crack propagated through the carbon/epoxy laminate in a 'stick-slip' manner, the crack advancing at finite increments, and crossed the battery with an unstable propagation along the whole battery length. The initial slope of the curves obtained from the laminates with

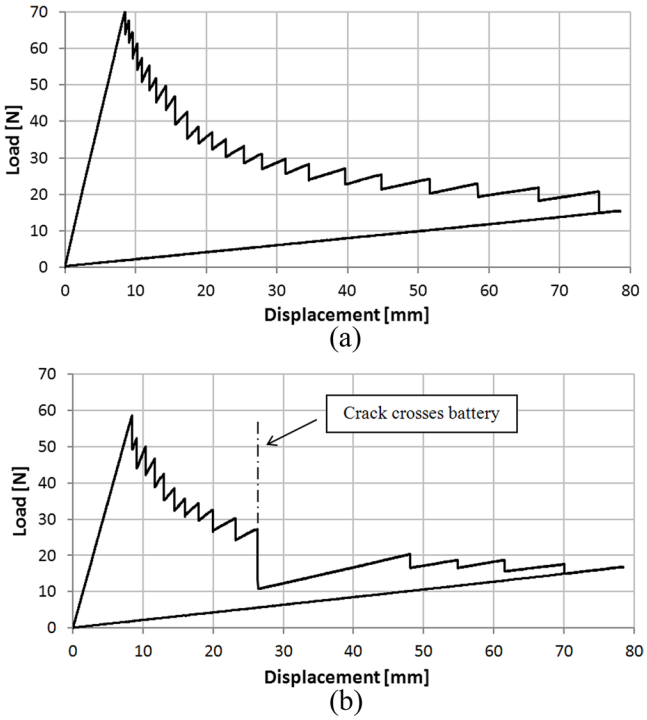

Figure 14. *Typical load-displacement profiles for double cantilever beam test (a) without embedded TFB and (b) with embedded TFB.*

embedded TFB was slightly lower than for those without, because the specimens with the embedded battery were 1.9 mm narrower than the nominal width. As expected from its low fracture toughness (Table 2), the crack propagated through the muscovite substrate for all the three test repetitions, splitting one of the two substrates along a cleavage plane, whereas the bond between the substrate and the carbon/epoxy composite remained intact, Figure 15. The average G_{IC} was reduced 15% by the presence of the battery, which was equal to the amount of crack surface occupied by the TFB, Table 4. This proved that the crack propagated through the battery without releasing a significant amount of strain energy.

The uniaxial mechanical tests gave evidence that the strain measured at the surface of a TFB-CFRP laminate with an embedded battery decreased sharply at the center of the specimen, where the TFB was located. An example of a full-field strain plot measured experimentally using DIC on the

Table 4. Average Mode I Fracture Toughness (G_{IC}) and Standard Deviation (σ) Resulting from Double Cantilever Beam (DCB) Testing.

	Average G_{IC} [J/m^2]	σ [%]
Specimens without TFB	315.5	2.27
Specimens with TFB	267.0	1.55
Specimens with TFB—net crack surface[1]	315.7	1.77

[1]Crack surface of thin film battery (TFB) is excluded from G_{IC} calculation

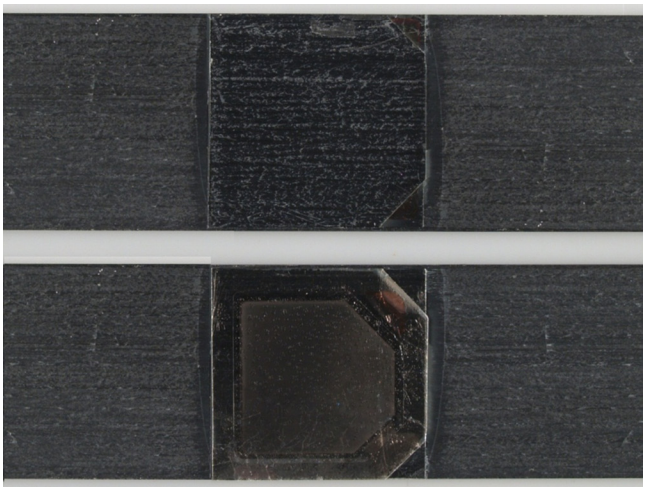

Figure 15. *Close-up image of crack surfaces after double cantilever beam.*

cross-ply laminate is shown in Figure 16. The corresponding strain field calculated by FEA is plotted in Figure 17 using consistent contour levels for comparison. The correlation between experiments and analysis was assessed based on the strain distribution along the longitudinal center-line of the specimen, identified by line a-a in Figure 16. The experimental and calculated strain values along line a-a are plotted in Figure 18. The FEA values are averaged corner outputs. Furthermore, the strain level predicted by the simplified CLT method is plotted as a constant strain throughout the nominal battery length and as a constant far-field strain elsewhere. A strain concentration factor, defined as the ratio between the average strain over the TFB ($\bar{\varepsilon}_{TFB}$) and the far-field strain (ε_0), was calculated for each of these data sets. The summary of the strain concentration factors for the tested lay-ups is reported in Table 5, showing a good agreement between the experimental and calculated strain field for all the stacking sequences. The results seem to confirm that the TFB shared load with the laminate as desired and that its adhesion to the CFRP material remained intact within the 3000 μstrain range. Moreover, the assumptions of plane stress and uniform strain through-the-thickness appear valid to predict the

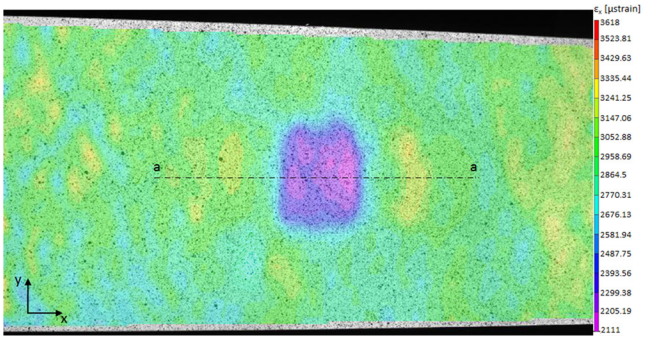

Figure 16. *Uniaxial mechanical tension test. Normal strain distribution in the loading direction (ε_x). Laminate stacking sequence at battery is (0/90/TFB/90/0). Applied far-field strain of 3107 μstrain.*

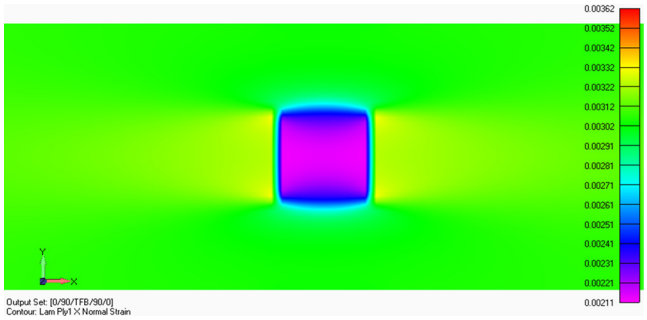

Figure 17. *Uniaxial mechanical tension test simulation. Strain distribution in the loading direction (x) calculated with finite element analysis (FEA). Laminate stacking sequence at battery is (0/90/TFB/90/0). Applied far-field strain of 3107 μstrain.*

Table 5. Uniaxial Mechanical Tension of Interlaminar TFB Embedding with Full-field Strain Monitoring. Measured and Calculated Normal x-Strain Concentration Factor Along Line a-a Shown in Figure 16. Factor is Defined as the Ratio Between Average TFB Strain $\bar{\varepsilon}_{TFB}$ and far-field strain ε_0.

	$\bar{\varepsilon}_{TFB}/\varepsilon_0$		
Lay-up	Experimental (DIC)	CLT	FEA (CLT)
(0/90/TFB/90/0)	0.75	0.66	0.71
(0_2/TFB/0_2)	0.84	0.79	0.81
(0/45/90/–45/TFB/–45/90/45/0)	0.80	0.74	0.80

overall elastic behavior of the laminate with an embedded battery. Within the limits of applicability of these assumptions, that is neglecting the three-dimensional stresses arising at lay-up transition, the interlaminar embedding did not lead to significant stress concentrations. In fact, the maximum stress concentration factor calculated with FEA was 1.07 and it occured in the $(0/90)_S$ laminate in proximity of the battery corners. This factor was calculated by dividing the maximum nodal strain in the *x*-direction by the far-field strain.

The same test procedure was adopted for the configuration with externally bonded TFB. The measured strain fields for the two tested lay-ups were characterized by higher strain gradients at the battery, in Figure 19. The highest gradient were located at the battery edges oriented transverse to the loading direction. These strain peaks were caused by a relative displacement between the upper substrate and the CFRP surface, which was detected as an apparent strain by the optical measurement instrumentation. Therefore, although this relative displacement was associated with a shear strain concentration in the sealant and in the adhesive, the normal strain peak had to be disregarded. The strain distribution over the battery, which coincides with the strain in the upper substrate, was in good agreement with the output of the shear lag model, Figure 20. As predicted by the analysis, the normal strain of the upper TFB substrate, which was zero at the battery edges, increased progressively up to a maximum at the center of the battery, without reaching the strain level predicted by the CLT. The high modulus mismatch between the adherents (substrates and CFRP sub-laminate) and the adhesives (sealant and adhesive film), as well as the relatively high thickness of the adhesives, were the causes of this extensive shear lag behavior. The calculated normal strain distributions in the adherents clearly show that the TFB length was not enough to allow for a uniform strain through-the-thickness, Figure 21. As a result, the upper substrate was affected by shear lag for the entire battery length, while the lower substrate and the CFRP sub-laminate reached a uniform strain at about one-third of the battery length. According to the shear lag model, the uniform strain region, defined as the area where the strain in the upper substrate reached at least 95% of the strain in the CFRP sub-laminate, began at a distance of 13.3 mm and 12.8 mm from the TFB edges for the $[(0/45/90/–45)_S$/AF/TFB] and (0_8/AF/TFB) laminates. Thus, in the shear lag region, which was as wide as 85 times the thickness of the battery and located next to the battery edge, the assumption of plane stress does not apply. For a sufficiently long TFB this edge effect would neg-

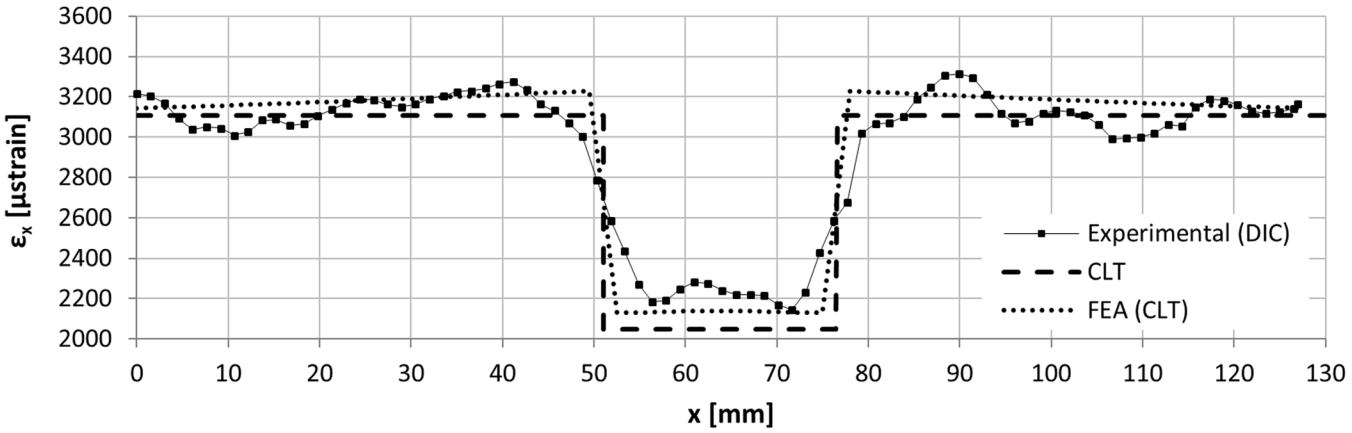

Figure 18. *Measured and calculated ε_x strain distribution along line a-a shown in Figure 16. Laminate stacking sequence at battery is (0/90/TFB/90/0).*

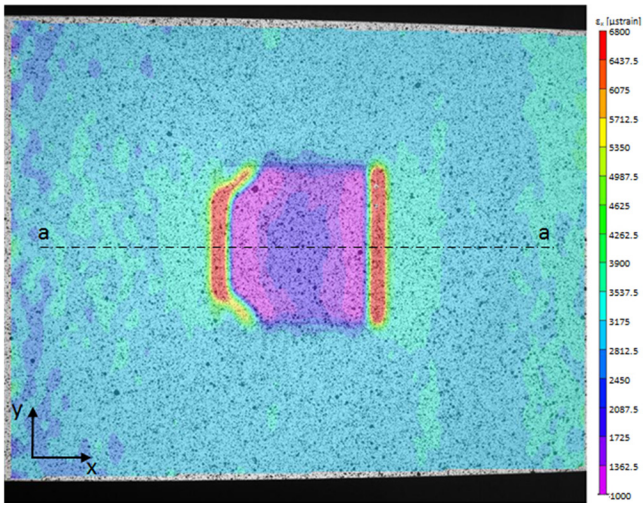

Figure 19. *Uniaxial mechanical tension test. Normal strain distribution in the loading direction (ε_x). Laminate stacking sequence at battery is [(0/45/90/–45)$_S$/AF/TFB]. Applied far-field strain of 3123 µstrain.*

ligibly reduce the load sharing efficiency of the externally bonded battery, however the three-dimensional stress-strain field poses challenges for the mechanical integrity and it is a fundamental knowledge required for the design of the TFB-CFRP laminate. The shear stress peak in the sealant occured at the battery edges, but the shear lag region extended well over the active components, Figure 22, and could trigger a mode II delamination onset at the edge of the active components, which is a known weak spot (Figure 6 and Figure 7).

Although the low sealant modulus was responsible for the extensive shear lag region, it had the advantage of leading to a low shear stress concentration factor, defined as the ratio between the peak stress and the average absolute value of the shear stress in the sealant layer. Shear stress concentration factors of 2.9 and 2.7 were calculated in the quasi-isotropic and in the unidirectional laminates, the latter being lower because the higher stiffness of the CFRP sub-laminate allowed a more gradual load transfer to the TFB. The shear stress concentration factors in the adhesive film, which had a higher modulus than the sealant, were 5.7 and 5.2 respectively.

The failure of the externally bonded battery configuration under uniaxial mechanical tension occured at an average applied far-field strain of 4898 µstrain, Table 6. This value was less than 50% of the CFRP sub-laminate critical strain. The same failure mode occurred in both the lay-ups and is attributable to the failure of the battery lower substrate. Micrographs of the failed specimens demonstrated that the interface between the adhesive film and the substrate remained intact, while the failed substrate showed multiple delaminations along the cleavage planes in proximity of the interface with the adhesive film. The unstable growth of one of these delaminations caused the battery to suddenly detach from the CFRP sub-laminate, leading to a brittle type of failure, Figure 23. The onset location of the failure can only be speculated. From the analysis of the calculated stress-strain fields it was noted that both specimens failed when the maximum shear stress occurring in the lower substrate reached 42.5 MPa, Table 6. Moreover, the TFB demonstrated during the electromechanical tension tests the capability to withstand higher normal strains than the ones calculated at failure for the externally bonded battery configuration and reported in Table 6. For these reasons a shear dominated failure starting from the substrate ends is deemed more likely than a failure caused by the peak normal stress occurring at substrate mid-span.

The results for the battery thickness increase during charging are reported in Figure 24. The small displacements involved were comparable to the sensitivity of the measuring instrumentation, therefore the surface data was affected by a fairly high amount of noise, Figure 24(a). The imprint of the anode shape in the contoured data shows that the thickness

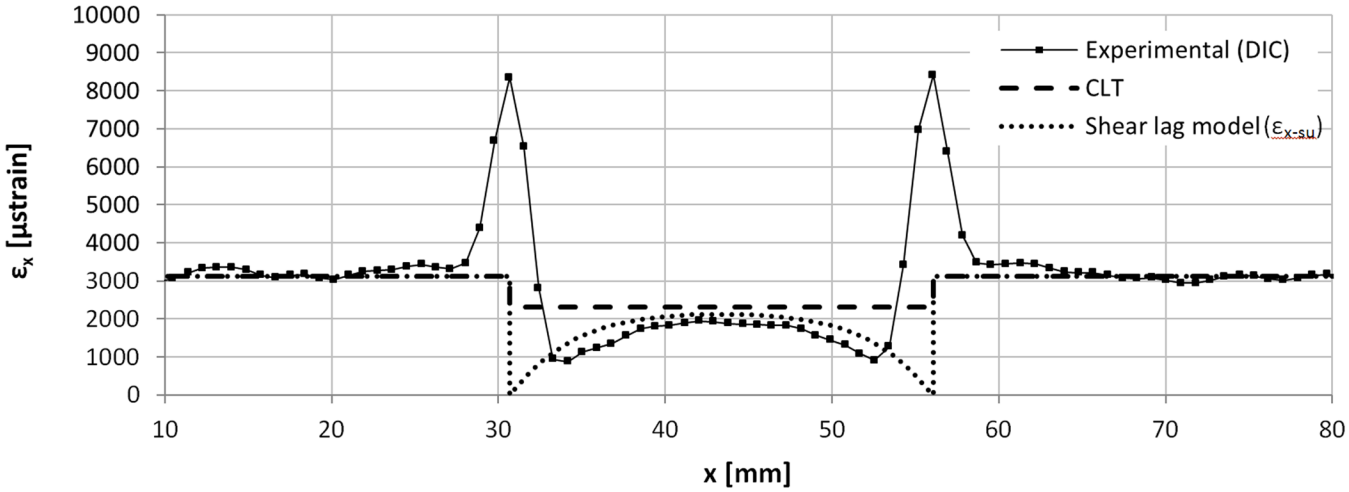

Figure 20. *Measured and calculated ε_x strain distribution along line a-a shown in Figure 19. Laminate stacking sequence at battery is [(0/45/90/–45)$_S$/AF/TFB]. The x-coordinate defined in Figure 13 is offset in order to match the DIC coordinate system.*

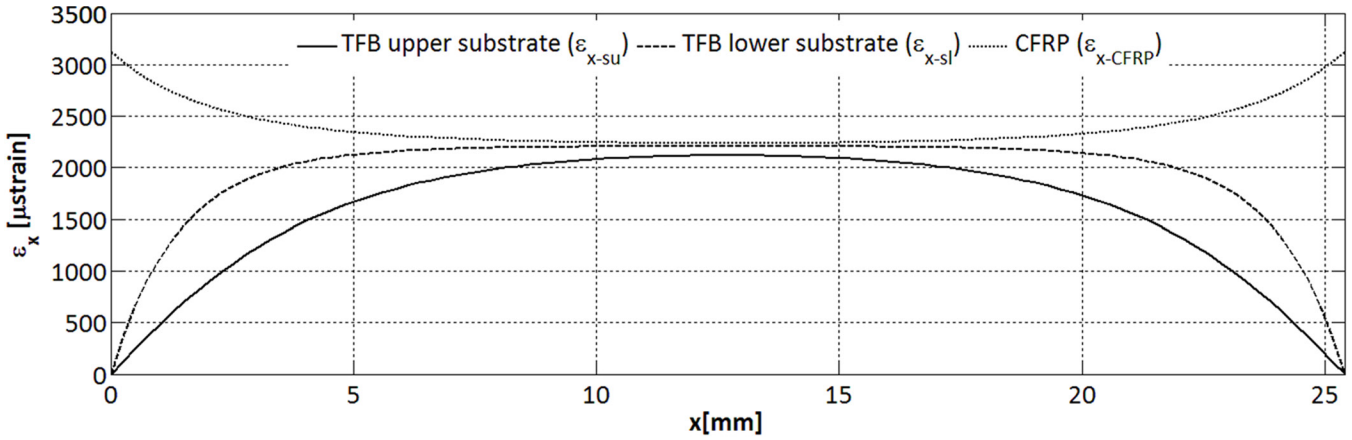

Figure 21. *Normal strain distribution in CFRP laminate and TFB substrates calculated with the shear lag model. Laminate stacking sequence at battery is [(0/45/90/–45)$_S$/AF/TFB]. Applied far-field strain of 3123 μstrain.*

increase was higher over the active components. In order to reduce the scatter, the average displacement of the area over the anode was calculated for every sampled displacement fields and plotted in Figure 24(b) as a function of the charge level. The charge level was defined as a linear function of the battery voltage during charging: 0% corresponded to the initial charging voltage and 100% to the voltage at the end of the charging process (i.e. when the charge current dropped below 50 μA). The thickness increase at full charge resulting from regression analysis of the averaged displacement data was about 4 μm. An influence from temperature variability is excluded since no significant environmental changes or battery self-heating was detected by the IR camera during the test. The perturbation introduced by a 4 μm battery cyclic expansion in terms of normal interlaminar stress and its long term effects on the integrity of the TFB-CFRP laminate are unknown at this stage of the research. However, the high coefficient of expansion demonstrated by a single TFB cell suggests that the design of future stacked multicell laminates should account for the thickness variability.

The uniaxial tension tests with capacity monitoring confirmed that the battery electrochemical performance is unaffected by the applied strain, as reported by [21,24,25]. The sequence of capacity measurements under increasing strain for one of the two specimens tested is shown in Figure 25 and demonstrates that the ability of the battery to store energy remained constant up to the electrical failure. Also the current and voltage profiles were unchanged until electrical failure occured. Failures consisted of an immediate and total loss of capacity that occured as soon as a certain strain level was exceeded. The discharge voltage measured at the beginning of the strain interval was lower than 3 V, therefore the charge/discharge circuit recorded a zero discharge capacity and switched to the charging mode. Once in charging mode, the current saturated the power supply output and remained constant at 5 mA, similar to a short circuit. The charge capacity relevant to this type of failure is reported as infinite in Figure 25. Bringing the strain back to zero did not restore the battery functioning and failure was confirmed.

The electrical failure occured when the strain at the bat-

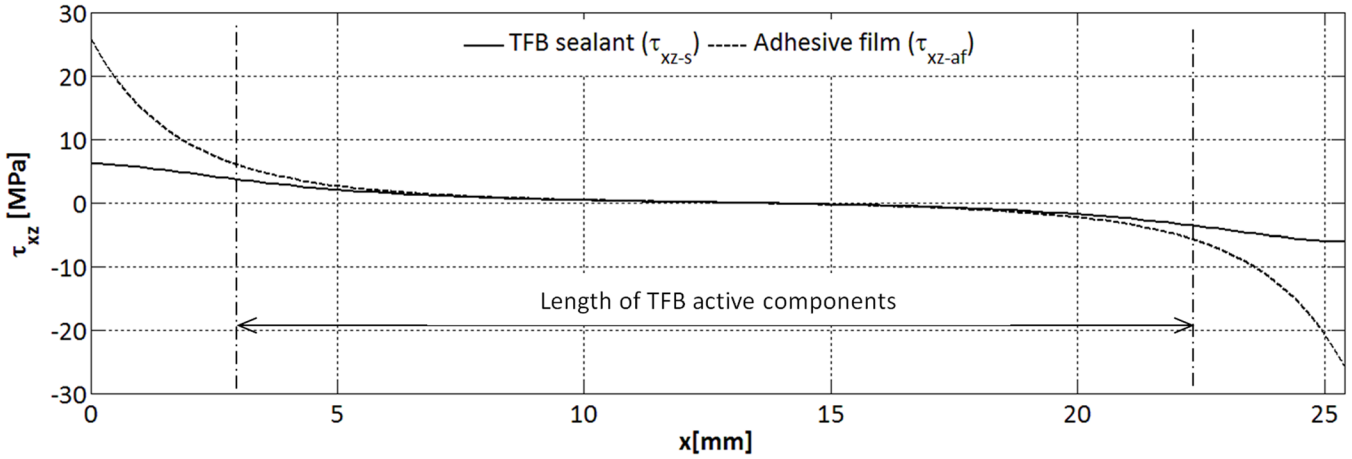

Figure 22. *Shear stress distribution in adhesive film and sealant calculated with the shear lag model. Laminate stacking sequence at battery is [(0/45/90/–45)$_S$/AF/TFB]. Applied far-field strain of 3123 μstrain. The length occupied by the active components is indicated in the plot area.*

Table 6. Uniaxial Mechanical Tension of Externally Bonded TFB. Summary of Critical Stress-strain Values at TFB Mechanical Failure. The Far-field Strain is Experimentally Measured, the Other Values are Calculated.

	Strain at Failure		Stress at Failure	
Lay-up	**Far-field ε_0 [μstrain]**	**Max. TFB $\varepsilon_{x-sl\,max}$ μstrain]**	**Max. TFB normal $\sigma_{x-sl\,max}$ [MPa]**	**Max. TFB shear $\tau_{xz-af\,max}$ [MPa]**
[(0/45/90/–45)S/AF/TFB]	5072	3588	639	42
(0_8/AF/TFB)	4724	4050	721	43
Average	4898	3819	680	42.5

tery exceeded 5100 μstrain. The critical strains reported in Table 7 are relevant to the last strain cycle preceding failure, thus they are maximum operating strain values. The strain at the battery was calculated by multiplying the far-field strain by the 0.8 strain concentration factor determined though the mechanical tests and FEA described in the preceding section, Table 5. The causes of the failure are unknown since the battery was not accessible for inspection and ultrasonic

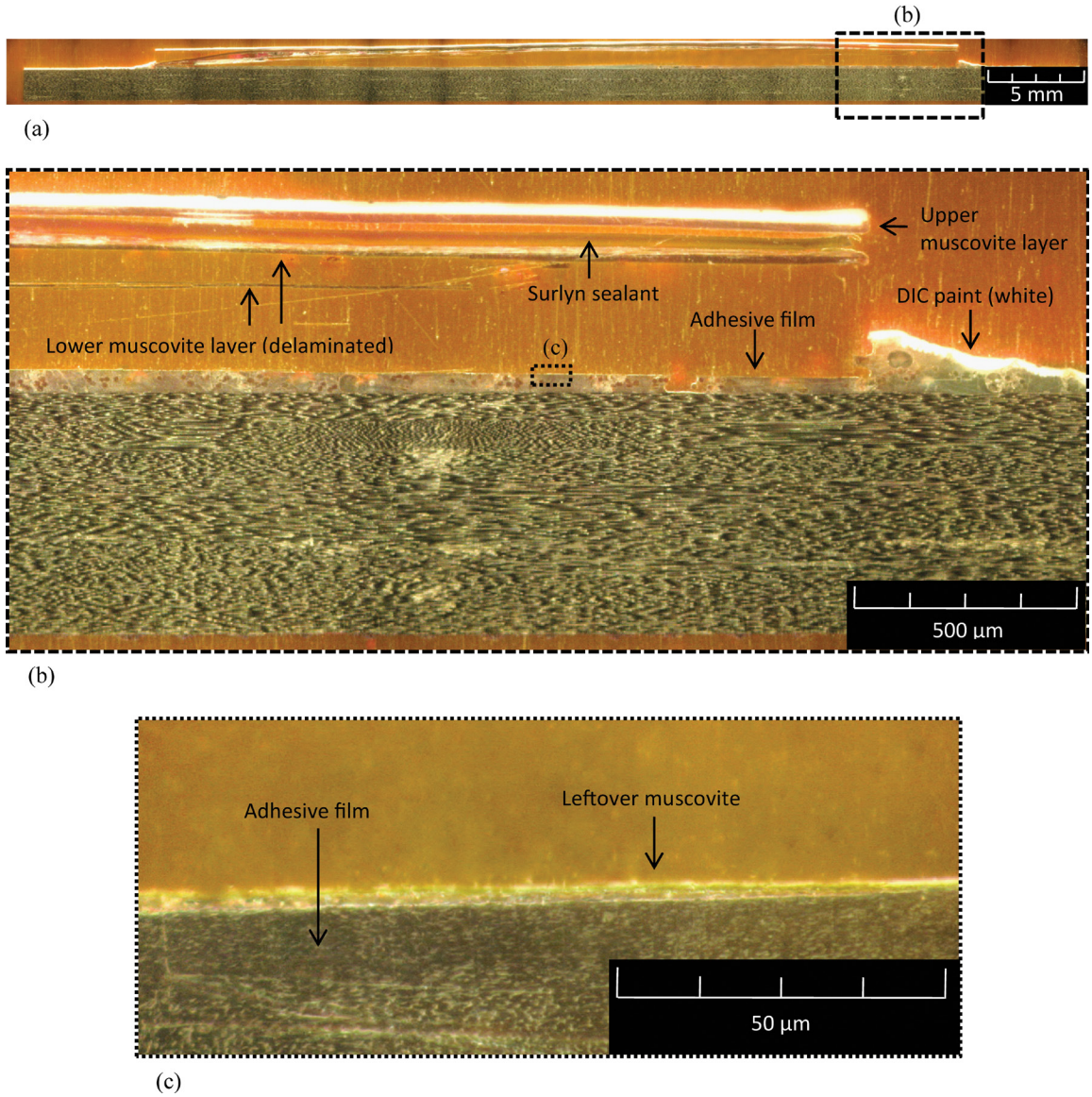

Figure 23. *Micrographs of the uniaxial tension test specimen with externally bonded TFB after failure. Laminate stacking sequence is (0_8/AF/TFB). (a) Full TFB section showing the battery lifted apart from the graphite laminate throughout the entire battery length. (b) Multiple delaminations propagate through the TFB substrate. (c) Adherent failure of the TFB substrate.*

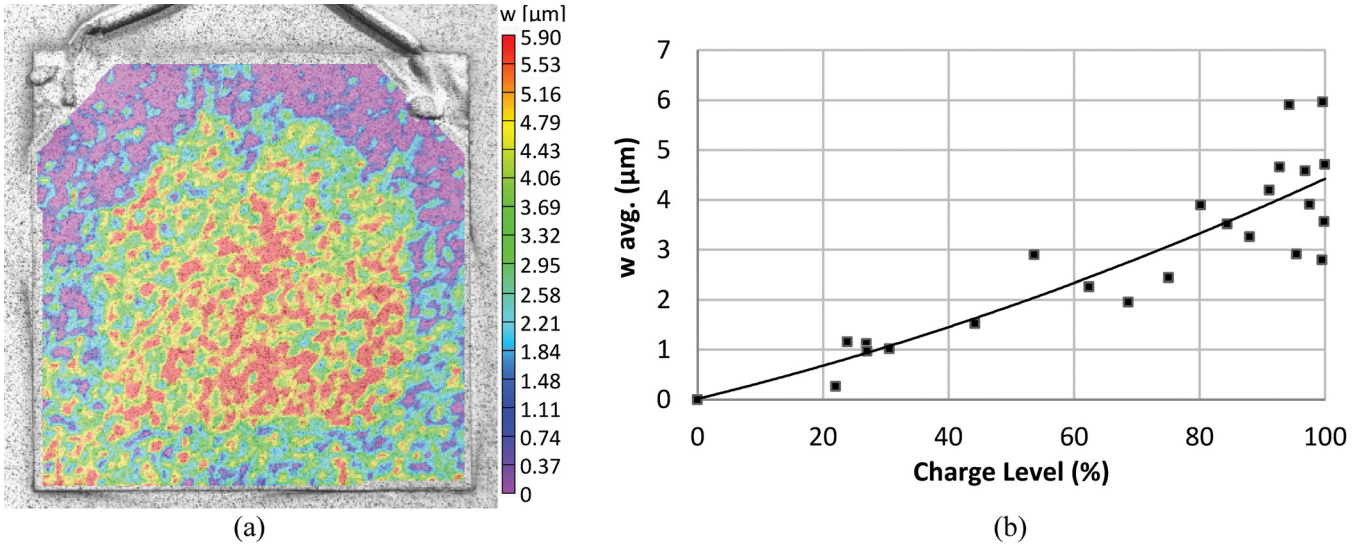

Figure 24. *(a) Anode side surface distribution of out-of-plane displacement w measured with digital image correlation (DIC) at 80% charge level. (b) Displacement w averaged over the anode area and second order polynomial regression of the data points.*

inspections had not proven to be effective for this particular structure. The in-plane stiffness of the specimens along the testing direction did not change significantly after the electrical failure occurred.

The results of the flexure tests showed that the applied curvature, similarly to the in-plane strain, does not affect the electrochemical performances up to failure. Results also gave evidence that the different combinations of strain and curvature lead to different failure modes. The specimens with an embedded battery at the laminate mid-plane and with a span-to-thickness ratio of 60:1 mechanically failed at a radius of curvature of 159 mm. The electrochemical performance remained constant up to the structural collapse of the laminate, which occured by compressive failure of the upper plies and was not affected by the presence of the battery. This was the only loading condition for which the laminate structural strength was more critical than the battery integrity, thereby showing that pure curvature of the TFB is not critical for most structural applications. In order to measure the critical radius of curvature of the battery, the span-to-thickness ratio was increased to a non-standard ratio of 145:1. This test set-up allowed achievement of the electrical failures, which occurred at an average radius of curvature of 112 mm, without being anticipated by performance fading and with the same sudden loss of discharge capacity experienced during the uniaxial tension test, Figure 26.

For the combined curvature and in-plane strain loading conditions, electrical failures were obtained at the 60:1 span-

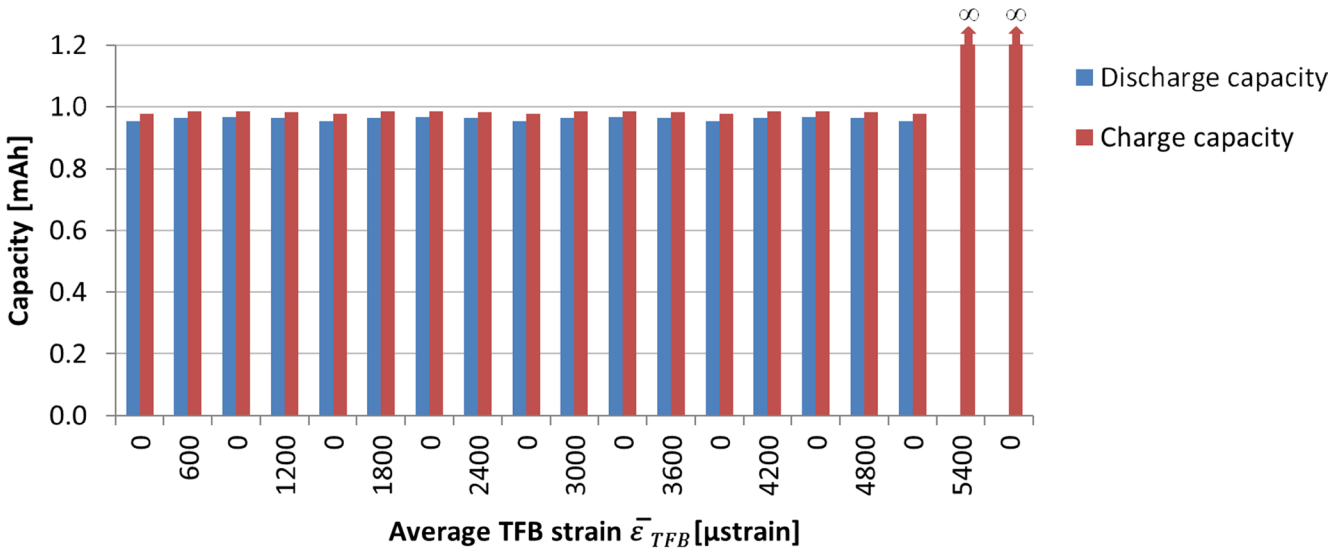

Figure 25. *Electrochemical characterization of the TFB-CFRP laminate under uniaxial mechanical tension. Capacity measured at increasing strain cycles up to failure. Laminate stacking sequence is (0/45/90/–45/TFB/–45/90/45/0).*

Table 7. Critical Strain Values for Uniaxial Mechanical Tension with TFB Electrical Capacity Monitoring of Laminate [0/45/90/–45/TFB/–45/90/45/0]. Measured Far-field Strain ε_0 and Corresponding Calculated Average TFB Strain $\bar{\varepsilon}_{TFB}$ at Electromechanical Failure.

	Strain at Electrical Failure	
Lay-up	ε_0 [μstrain]	$\bar{\varepsilon}_{TFB}$ [μstrain]
Repetition 1	6000	4800
Repetition 2	6750	5400
Average	6375	5100

to-thickness ratios. The critical radii of curvature and strains are summarized in Table 8. The compressive loading condition, with a low far-field strain at failure of 2832 μstrain, was particularly critical. Failure occurred by delamination buckling of the TFB packaging, Figure 27, and subsequent battery contamination. The failure initiation is uncertain. It can be attributed to an adhesive failure at the sealant-substrate interface, or, given its low fracture toughness, to a delamination of the substrate. A cohesive failure of the sealant is deemed unlikely because of the relatively high fracture toughness of Surlyn. The buckling of the upper substrate, shown in a close-up view in Figure 28, opened a path for air and moisture ingression through the battery packaging and it was followed by a neutral grey discoloration of the anode occurring below the wrinkle of the substrate. This chromatic change was attributed to the reaction of lithium with contaminants. Like for the failure of the embedded battery, the discharge capacity measured after failure was considered zero because the discharge voltage was lower than 3 V. On the other hand, the charge current did not saturate the power supply as mentioned for the embedded battery, but it remained constant at about 0.45 mA and it showed a fairly high amount of random high frequency oscillations with approximately 50 μA of amplitude. The charging process was declared failed after one hour.

The specimens tested in curvature and positive strain

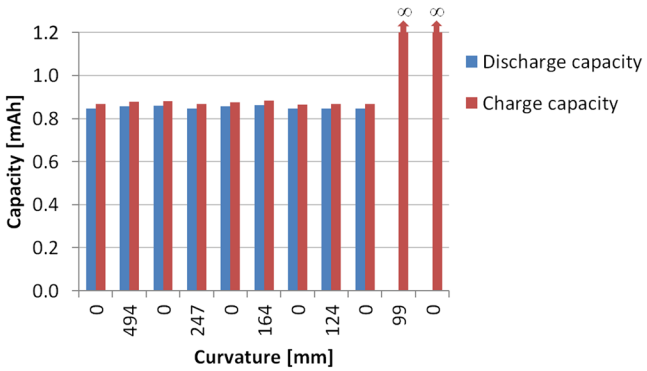

Figure 26. *Electrochemical characterization of the TFB-CFRP laminate under single curvature. Capacity measured at increasing curvature cycles up to failure. Laminate stacking sequence is [0/90/TFB/90/0].*

Table 8. Four Point Bending with TFB Electrical Capacity Monitoring. Summary of Critical Radius of Curvature and Strain at Electromechanical Failure.

		Radius of Curvature [mm]	Far-field Strain [μstrain]
Curvature	Repetition 1	124	0
	Repetition 2	99	0
	Average	112	0
Simultaneous curvature and negative in-plane strain	Repetition 1	504	–2971
	Repetition 2	557	–2692
	Average	531	–2832
Simultaneous curvature and positive in-plane strain	Repetition 1	204	7354
	Repetition 2	224	6683
	Average	214	7019

failed at an average radius of curvature of 214 mm and an average far-field strain of 7019 μstrain. The failure mode consisted of brittle fracturing of the lower substrate and battery detachment form the CFRP sub-laminate, as described for the externally bonded battery configuration subjected to uniaxial tension. Although the failure modes for these two loading conditions appeared to be the same, the critical far-field surface strain of the laminates tested in flexure was 40% higher. The cause for the mismatch is partially attributed to an error associated with the calculation of the strain at failure for the curvature and positive in-plane strain loading condition. In fact, the deflections of the specimens at failure were in excess of 10% of the support span, leading to geometrical nonlinearities. Therefore the small deformations assumption utilized for computing the strain provided overestimated values for this particular case.

4. CONCLUSIONS

The assumptions of plane stress and uniform normal strain through-the-thickness allowed the prediction of the overall elastic behavior of the hybrid thin film lithium ion—graphite battery laminates subjected to in-plane strain, for

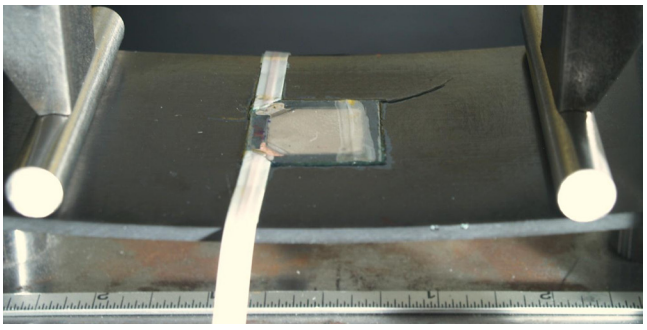

Figure 27. *Failure of TFB undertaking electromechanical flexure testing. Delamination buckling of the battery at a radius of curvature of 504 mm and compressive strain of 2971 μstrain.*

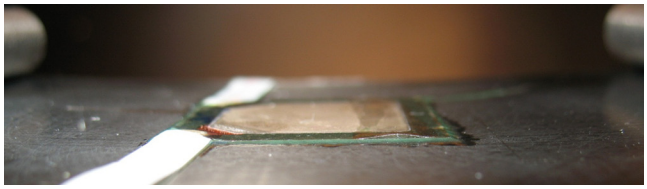

Figure 28. *Failed battery shown in Figure 27 reveals air and moisture path through the buckled substrate.*

either the embedded battery or the externally bonded battery configuration. However, besides not being applicable at lay-up transition, these assumptions did not capture the extensive shear-lag that develops in proximity of the battery edges of the externally bonded battery configuration. Therefore three-dimensional FEA or higher order laminate, zig-zag, or layerwise theories are required for an optimized design.

The operational envelope for the hybrid laminate featuring the current thin film battery technology is reduced with respect to a conventional CFRP structural laminate. The failure of the TFB-CFRP laminate, defined as the mechanical failure of any laminate component or the electrical failure of the battery, occured at an applied far-field strain of 4898 μstrain for uniaxial tension and 2832 μstrain for uniaxial compression in the worst case scenarios. The ability to tolerate curvature was equivalent to that of a conventional laminate as long as the battery was located at the laminate mid-plane and provided that the critical radius of curvature of 112 mm was not exceeded. Within these operational limits the electrochemical performance was not affected by the mechanical boundary conditions. Differences between the embedded battery and the externally bonded battery configuration were discussed in detail.

The critical failure modes of the externally bonded battery configuration included mode II dominated delamination or disbonding of the battery packaging when the laminate was subjected to mechanical tension, with failure onset at the battery edges or possibly at the edge of the active components. Delamination buckling of the battery upper substrate was critical under compressive loading. The packaging buckling failure triggered the electrical failure by cell contamination with air and moisture. The delamination or cracking of the active components were not critical failure modes with the current packaging materials. Hence the battery packaging was the weakest link for the structural and electrical integrity.

The critical failure modes for the embedded battery configuration were not identified. The test campaign gave evidence that electrical failure is more critical than mechanical failure of the laminate for the in-plane strain loading condition. Battery substrate splitting with subsequent tearing of the active components, delamination of the packaging with cell contamination, or mechanical failure of the active components are all possible failure modes. The failure of the electrical connections is excluded because the battery discharge voltage remained detectable after failure. The same uncertainties apply to the electrical failure under curvature, which is, however, less critical than the mechanical failure of the laminate.

The low fracture toughness of the muscovite substrate is the most important limiting factor for the mechanical integrity of the current battery packaging. The high modulus mismatch between the Surlyn sealant and the substrate is the second most important limiting factor. The delamination of the substrate was responsible for the failure of the externally bonded battery under in-plane tension and is suspected to be the main cause for the delamination buckling that occured under compression. The low fracture toughness of the substrate might have concealed other shortcomings such as poor mechanical strength of the electrodes and electrolyte and their bonding interfaces with the packaging, which were expected to be the critical for electromechanical survivability. A higher modulus sealant would increase the load sharing efficiency of the externally bonded battery and prevent compression buckling of the packaging. On the other hand, it would also increase the shear stress concentration factor at the battery edges, which promotes disbonding onset.

The interlaminar embedding of the battery did not have direct detrimental effects on the CFRP laminate elastic properties and mechanical strength. Perfect bonding and predictable load sharing with the composite structure up to failure were observed. Nevertheless the possible delamination onset and propagation at lay-up transition requires further investigation. Moreover, accounting for the effects of the cyclic battery thickness variation upon the interlaminar normal stress and strain energy release rate is recommended for stacked multicell architectures. The stress induced by the battery thickness increase could be reduced by curing the laminates with fully charged batteries; however the study on manufacturability conducted by the authors revealed that thermal processing at full state of charge reduces the maximum curing temperature that the batteries can tolerate without permanent capacity loss. The design of TFB-CFRP laminates would benefit from the development of appropriate electrode materials that minimize volume variation during lithiation-delithiation.

The results demonstrate the importance of the packaging for the mechanical integration of batteries and structure. The laminate stress-strain field is highly influenced by the design of the substrate and sealant layer, as shown by the analysis of the uniaxial mechanical tension tests of the embedded and externally bonded battery configurations. Moreover, all the critical electromechanical failure modes that have been identified are initiated by the failure of a packaging component. For these reasons conventional packaging materials currently adopted by standard flexible electronics are inadequate for the multifunctional application. Lightweight aeronautical materials and high temperature structural composites developed for space application should be considered for

their high elastic modulus and the ability to withstand severe stress and the high temperature associate with the manufacturing of the battery.

Based on the current performance, this multifunctional technology could be applied to a limited range of micro- and mini-UAV platforms, where the mechanical demands are minimal and the ratio of batteries to structural composites can be large enough to provide the required electrical energy and maximize the multifunctional efficiency, More demanding applications require a technological transition to improve the mechanical properties of the electrochemically active components and the packaging. In order to support the design of the next generation of airborne structural thin film batteries, modeling of the three-dimensional stress-strain field, delamination initiation and propagation are required to increase the mechanical strength and the electric survivability of the multifunctional system. The design should also account for the constraints given by the physiochemical requirements of the TFB manufacturing process and by the composite laminate curing process. Finally, the density of the packaging materials should be minimized for lightweight design, whereas the current substrate material has a too high density of 2.6 g/cm^3.

ACKNOWLEDGMENTS

This research was sponsored by the U.S. Air Force Office of Scientific Research (AFOSR) within the 5-year MURI '06 Program "Energy Harvesting and Storage Systems and Their Integration to Aero Vehicles" AF-MURI (FA9550-06-1-0326) led by the University of Washington. The authors would like to acknowledge Dr. Byung-Lip "Les" Lee, AFOSR Program manager, and Prof. Minoru Taya, MURI PI.

References

[1] Thomas J.P., Qidwai M.A., Matic P., Everett R.K. (2002). Multifunctional structure-plus-power concepts, 43rd AIAA/ASME/ASCE/AHS/ASC Structures, Structural Dynamics, and Materials Conference, Denver, CO.

[2] Thomas J.P., Qidwai M.A. (2004). Mechanical design and performance of composite multifunctional materials, *Acta Materialia,* 52: 2155–2164. http://dx.doi.org/10.1016/j.actamat.2004.01.007.

[3] Thomas J.P., Qidwai M.A. (2005). The design and application of multifunctional structure–battery material systems, *Journal of the Minerals, Metals and Materials Society,* 57(3):18–24. http://dx.doi.org/10.1007/s11837-005-0228-5.

[4] Qidway M.A., Baucom J.N., Thomas J.P., Horner D.M. (2005). Multifunctional Applications of thin film Li polimer battery cells, *Material Science Forum,* 492–493: 157–162. http://dx.doi.org/10.4028/www.scientific.net/MSF.492-493.157

[5] Owens B.B. (2000). Solid state electrolytes: overview of materials and applications during the last third of the Twentieth Century, *Journal of Power Sources,* 90: 2–8. http://dx.doi.org/10.1016/S0378-7753(00)00436-5.

[6] Liu E., Sherman E., Jacobsen A. (2008). Design and fabrication of multifunctional structural batteries, *Journal of Power Sources,* 189(1): 646–650. http://dx.doi.org/10.1016/j.jpowsour.2008.09.082.

[7] Snyder J.F., Wong E.L., Hubbard C.W. (2009). Evaluation of commercially available carbon fibers, fabrics and papers for potential use in multifunctional energy storage applications, *Journal of the Electrochemical Society,* 156(3): 215–224. http://dx.doi.org/10.1149/1.3065070.

[8] Xu C., Ma C., Taya M. (2008). Electrolyte for Laminated Polymer Lithium Rechargeable Battery. *Electroactive Polymer Actuators and Devices (EAPAD),* Proc. Of SPIE Vol. 6927, 692714. http://dx.doi.org/10.1117/12.778705.

[9] Snyder J.F., Carter R.H., Wetzel E.D. (2007). Electrochemical and mechanical behavior in mechanically robust solid polymer electrolytes for use in multifunctional structural batteries, *Chemistry of Materials,* 19(3): 3793–3801. http://dx.doi.org/10.1021/cm070213o.

[10] Snyder J.F., Wetzel E.D., Watson C.M. (2009). Improving multifunctional behavior in structural electrolytes through copolymerization of structure- and conductivity-promoting monomers, *Polymer,* 50: 4906–4916. http://dx.doi.org/10.1016/j.polymer.2009.07.050.

[11] Wetzel E.D. (2011). Structural composite capacitors, supercapacitors and batteries. Presented at the Air Force Office of Scientific Research (AFOSR) Annual Grantees/Contractors Meetting, Mechanics of Multifunctional Materials & Microsystems, Arlington, VA, August 1–5.

[12] Whittingham M.S. (2004). Lithium batteries and cathode materials, *Chemical Reviews,* 104(10): 4271–4301. http://dx.doi.org/10.1021/cr020731c. PMid:15669156.

[13] Whittingham M.S., Song Y., Lutta S., Zavalij P.Y., Chernova N.A. (2005). Some transition metal (oxy)phosphates and vanadium oxides for lithium batteries, *Journal of Material Chemistry,* 15: 3362–3379. http://dx.doi.org/10.1039/b501961c.

[14] Wang Y., Cao G. (2008). Developments in nanostructured cathode materials for high-performance lithium-ion batteries, *Advanced Materials,* 20: 2251–2269. http://dx.doi.org/10.1002/adma.200702242.

[15] Chan C.K., Peng H., Liu G., McIlwrath K., Zhang X.F., Huggins R.A., Cui Yi (2008). High performance lithium battery anodes using silicon nanowires, *Nature Nanotechnology* 3: 31–35. http://dx.doi.org/10.1038/nnano.2007.411. PMid:18654447.

[16] Trevey J.E., Wang J., DeLuca C.M., Maute K.K., Dunn M.L., Lee S.H., Bright V.M. (2011). Nanostructured silicon electrodes for solid-state 3-d rechargeable lithium batteries, *Sensors and Actuators A: Physical,* 167: 139–145. http://dx.doi.org/10.1016/j.sna.2011.02.015.

[17] Scott I.D., Jung Y.S., Cavanagh A.S., Yan Y., Dillon C.A., George S.M., Lee S.H. (2011). Ultrathin coatings on nano-$LiCoO_2$ for FaLi-ion vehicular applications, *Nano Letters,* 11: 414–418. http://dx.doi.org/10.1021/nl1030198. PMid:21166425.

[18] Liu Y., Taya M. (2009). Electrospinning fabrication and electrochemical properties of lithium cobalt nanofibers for lithium battery cathode, *Active and Passive Smart Structures and Integrated Systems*. Proc. Of SPIE Vol. 7288 728806-1. http://dx.doi.org/10.1117/12.816173.

[19] Son S.B., Trevey J.E., Roh H., Kim S.H., Kim K.B., Cho J.S., Moon J.T., DeLuca C.M., Maute K.K., Dunn M.L., Han H.N., Oh K.H., Lee S.H. (2011). Microstructure study of electrochemically driven LixSI, *Advanced Energy Materials,* 1: 1199–1204. http://dx.doi.org/10.1002/aenm.201100360.

[20] DeLuca C.M., Maute K., Dunn M.L. (2011). Effects of electrode particle morphology on stress generation in silicon during lithium insertion, *Journal of Power Sources,* 196: 9672–9681. http://dx.doi.org/10.1016/j.jpowsour.2011.07.035.

[21] Golmon S., Maute K., Dunn M.L. (2009). Numerical modeling of electrochemical–mechanical interactions in lithium polymer batteries, *Computers and Structures* 87: 1567–1579. http://dx.doi.org/10.1016/j.compstruc.2009.08.005.

[22] Pereira T., Scaffaro R., Nieh S., Arias J., Guo Z., Hahn H.T. (2006). The performance of thin-film Li-ion batteries under flexural deflection, *Journal of Micromechanics and Microengineering,* 16: 2714–2721. http://dx.doi.org/10.1088/0960-1317/16/12/026.

[23] Pereira T., Scaffaro R., Nieh S., Arias J., Hahn H.T. (2008). Performance of thin-film Lithium Energy cells under uniaxial pressure, *Advaced Engineerig Materials,* 10(4): 393–399. http://dx.doi.org/10.1002/adem.200700214.

[24] Pereira T., Scaffaro R., Nieh S., Arias J., Hahn H.T. (2008). Embedding thin-film lithium energy cells in structural composites, *Composites Science Technology,* 68/7-8: 1935–1941. http://dx.doi.org/10.1016/j.compscitech.2008.02.019.

[25] Pereira T., Scaffaro R., Nieh S., Arias J., Hahn H.T. (2009). Energy storage structural composites: a review, *Journal of Composite Materials,* 43/5: 549–560. http://dx.doi.org/10.1177/0021998308097682.

[26] Luongo C.A., Masson P.J., Nam T., Mavris D., Kim H.D., Brown D.V., Waters M., Hall D. (2009). Next generation more-electric aircraft: a potential application for HTS superconductors, *IEEE Transactions on Applied Superconductivity,* 19 (3): 1055–1068. http://dx.doi.org/10.1109/TASC.2009.2019021

[27] Bates J.B., Dudney N.J., Gruzalsky G.R., Zuhr R.A., Choudhury A., Luck C.F., Robertson J.D. (1992). Electrical properties of amorphous lithium electrolyte thin films, *Solid State Ionics,* 53-56: 647–654. http://dx.doi.org/10.1016/0167-2738(92)90442-R.

[28] Bates J.B., Dudney N.J., Neudecker B., Ueda A., Evans C.D. (2000). Thin film lithium and lithium-ion batteries, *Solid State Ionics,* 135: 33–45. http://dx.doi.org/10.1016/S0167-2738(00)00327-1

[29] Bates, J.B., Dudney, N.J., Neudecker, B.J., Hart, F.X., Jun, H.P. and Hackhey, S.A. (2000). Preferred orientation of Polycrystalline $LiCoO_2$ films, *Journal of the Electrochemical Society,* 147(1): 59–70. http://dx.doi.org/10.1149/1.1393157.

[30] Krasnov, V., Nieh, K. and Li, J. (2011). Thin film battery and manufacturing method, US Patent No. 7862927. http://dx.doi.org/10.1088/0960-1317/12/1/309.

[31] Krasnov, V., Nieh, K., Ting, S., Tang, P., Chang, F. and Lin C. (2005). Sputter deposition of lithium phosphorous oxynitride material, US Patent No. 6863699.

[32] West W.C., Whitacre J.F., White V., Ratnakumar B.V. (2002). Fabrication and testing of all solid-state microscale lithium batteries for microspacecraft applications, *Journal of Micromechanics and Microengineering,* 12: 58–62.

[33] McNeil L.E., Grimsditch M. (1993). Elastic moduli of muscovite mica, *Journal of Physics: Condensed Matter,* 5: 1681–1690. http://dx.doi.org/10.1088/0953-8984/5/11/008.

[34] ASTM D5528 – 01. Standard test method for mode I interlaminar fracture toughness of unidirectional fiber-reinforced polymer matrix composites.

[35] ASTM D3039/D3039M – 08. Standard test method for tensile properties of polymer matrix composite materials.

[36] ASTM 6272 - 10. Standard test method for flexural properties of unreinforced and reinforced plastics and electrical insulating materials by four-point bending.